Fibre Optical Ice Sensing: Modelling and Measurement-Based Characterization

Master Thesis

Alexander Siegl

Institute of Electrical Measurement and Measurement Signal Processing
Graz University of Technology

Supervisor: Dipl.-Ing. Dr.techn. Markus Neumayer

Graz, September 2019

Abstract

Atmospheric ice growth can be a potential hazard for structures like high-voltage lines, wind turbines or antennas in alpine regions. Fibre optical ice sensing is a possible approach to detect and monitor ice accretion. The sensing principle is based on the optical coupling between single glass fibre bundles due to the accreted ice. Recent publications show the feasibility of ice monitoring with this approach by means of experimental studies. In this thesis the properties and capabilities of fibre optical sensing for ice detection and thickness measurement are investigated by means of sensor modelling and sensor simulation, as well as dedicated measurements using a prototype. A new sensor model is developed, which includes all relevant interactions between the sensor and the ice accretion process. Simulations for different ice types are performed where the random nature of the ice accretion process is considered. The construction of a sensor prototype is presented and a measurement-based characterization of this sensor is performed. Based on the measurements and the model, the capability to detect the begin of the ice accretion is analysed. As for the determination of the ice thickness, an uncertainty analysis is presented.

Kurzfassung

Wetterbedingter Eisbesatz kann vor allem in alpinen Regionen eine potenzielle Gefahr für Bauten wie Hochspannungsleitungen, Windräder oder Antennen darstellen. Faseroptische Sensorik ist ein möglicher Ansatz diesen Eisbesatz zu erfassen und seine Dicke zu messen. Das Prinzip hinter diesen Sensoren beruht auf der optischen Kopplung zwischen einzelnen Glasfaserbündeln und dem angewachsenen Eis. Die Anwendbarkeit des Verfahrens wurde in mehreren Publikationen auf Basis von experimentellen Untersuchungen gezeigt. In dieser Arbeit werden die Eigenschaften und Möglichkeiten der faseroptischen Eissensorik bezüglich der Eisdetektion und Dickenmessung untersucht. Die Untersuchung erfolgt auf Basis von simulationsbasierten Analysen und einer messtechnischen Charakterisierung. Ein neu entwickeltes Sensormodell berücksichtigt dabei alle relevanten Effekte zwischen dem Sensor und dem Eisbesatz. Die Möglichkeit Eis zu detektieren wird anhand der messtechnischen Charakterisierung von Prototypen demonstriert. Für die Bestimmung der Eisdicke wird eine Unsicherheitsanalyse präsentiert.

EIDESSTATTLICHE ERKLÄRUNG

Ich erkläre an Eides statt, dass ich die vorliegende Arbeit selbstständig verfasst, andere als die angegebenen Quellen/Hilfsmittel nicht benutzt, und die den benutzten Quellen wörtlich und inhaltlich entnommene Stellen als solche kenntlich gemacht habe.

Graz, am …… ……..
(Unterschrift)

STATUTORY DECLARATION

I declare that I have authored this thesis independently, that I have not used other than the declared sources / resources, and that I have explicitly marked all material which has been quoted either literally or by content from the used sources.

…… ……..
date (signature)

Acknowledgement

First of all, I would like to thank my supervisor Markus Neumayer for his commitment and his support.

I also thank Stefan Veitsberger for his support and advice regarding the mechanical tasks in the course of writing this thesis.

Special thanks also go to my family and my colleagues at the institute.

Graz, September 2019 Alexander Siegl

Contents

1 Introduction **1**
- 1.1 Natural Ice Accretion Process . . . 5
- 1.2 Fibre Optical Ice Sensing . . . 6
- 1.3 Thesis Outline . . . 8

2 Review of Fibre Optical Ice Sensing **9**
- 2.1 Basic Sensing Principle of the FOIS . . . 9
  - 2.1.1 Ice Types . . . 14
- 2.2 Overview of FOIS . . . 15

3 Simulation Framework for FOIS **17**
- 3.1 Effects for Sensor Modelling . . . 18
  - 3.1.1 Refractive Index . . . 19
  - 3.1.2 Law of Reflection . . . 19
  - 3.1.3 Law of Refraction . . . 21
  - 3.1.4 Fresnel Equations . . . 22
  - 3.1.5 Total Internal Reflection . . . 26
  - 3.1.6 Beer-Lambert Law . . . 27
  - 3.1.7 Fibre Optics . . . 30
- 3.2 Sensor Model and Simulation Steps . . . 32
  - 3.2.1 Sensor Model . . . 32
  - 3.2.2 Derivation at Interfaces . . . 34
  - 3.2.3 Discretization in z-Direction . . . 39
- 3.3 Ray-Tracer versus Conventional Approach . . . 39
- 3.4 Simulation of Different Ice Types . . . 41
  - 3.4.1 Glazed Ice . . . 41
  - 3.4.2 Rime Ice . . . 42

4 Construction of a Sensor **45**
- 4.1 Merging of the Bundles . . . 47
- 4.2 Stabilizing and Compressing of the Bundles . . . 48
- 4.3 Mounting of the Metallic Sheath . . . 49
- 4.4 Sealing and Polishing . . . 49
- 4.5 Electronic Components . . . 53
  - 4.5.1 Phototransitor . . . 53

4.5.2 Light Emitting Diode 57

5 Study and Analysis of the Sensor Effect and the Sensor Behaviour 60
5.1 Measurement Setup and Ice Accretion 60
5.1.1 Measurement Setup 60
5.1.2 Ice Accretion 63
5.2 Experiments 66
5.2.1 Study: Glazed Ice 66
5.2.2 Study: Rime Ice 71
5.2.3 Cross-Sensitivity 73
5.3 Simulation and Model Calibration 75
5.3.1 Surface Deviation and Diffuse Reflection 75
5.3.2 Ice Types 75
5.3.3 Glazed Ice 78
5.3.4 Rime Ice 81
5.4 Uncertainty Evaluation for Thickness Measurement 83

6 Conclusion and Outlook 85
6.1 Conclusion 85
6.2 Outlook 87

Bibliography 88

1 Introduction

Technical structures have to withstand several ambient influences, without losing their mechanical functionality. Especially structures or buildings in the outdoors have to brave wind, rain and heat. Another weather event is atmospheric ice formation. Structures in alpine regions, like power transmission lines [1, 2] or wind turbines [3], are endangered by natural ice accretion. The accreted ice is a potential hazard for the structures itself as the mass of the accreted ice stresses the mechanical stability. This stress can lead to mechanical failure and can cause danger for the structure itself. A typical example of this is ice formation on a power line. If the additional load on the support towers or the lines is too heavy, the entire tower could collapse or the lines might be torn out of their anchoring. Besides the structural damage, also human beings can be harmed by ice accreted on structures next to or above streets. Cars or even pedestrians are in danger of getting hit by dropping ice. Figure 1.1 shows a scenario where the accreted ice has been fallen onto a street.

Figure 1.1: Dropped ice mass from a power transmission line onto a street. The dropping of ice is a potential hazard for humans and cars in the vicinity of the road [4].

Early and reliable ice detection can prevent an incident as depicted above. For the ice monitoring, a proper sensor is required.

The sensor has to be capable of

- detecting early ice accretion and
- measuring the ice thickness.

Regarding the detection, the sensor has to distinguish between water and ice. Once the ice is detected, easy countermeasures can be triggered when a possible ice accretion arises. For power lines, the electric load could be increased leading to a warming of the line. If that is not possible, the accreted ice has to be removed by humans causing again additional danger as they have to climb on towers [4].

In order to monitor ice, different sensing effects can be used. An overview of common ice sensing principles is presented in [5] and [6]. Some of the principles are listed in Figure 1.2 and assessed regarding their capabilities of detecting and measuring ice thickness.

Sensor principle	Principle	Spatial Coverage	Sensor Characteristics				Ref.
			Response time / detection	Ice thickness	Load	Complexity/Hardware effort	
Capacitive	Electric field to determine the presence of dielectric materials	local	Early detection of icing with high probability	from 0.1 mm to > 10 mm (range), 1mm precision	-	minor, low power circuitry	[7]
Impedance	Complex impedance measurement	local	early detection	0.1 mm to 5 mm (range)	distinguish between water and ice	moderate, spectroscopy measurement system	[10]
Vision	Camera based measurement system	medium	moderate to high, depending on type of ice (rime, glaze)	moderate	-	high system effort	[11]
Optical	Fiber Bragg gratings	medium	low	high	-	cross sensitivity to strain (e.g. wind), temperature, EMC immunity	[12]
Microwave	microwave energy reflected from ice layers	local	moderate	moderate	-	moderate, energy demanding	[6]

Figure 1.2: Overview and assessment of ice sensing principles adapted from [5].

In general, ice sensing principles can be divided into direct ice sensing and indirect ice sensing approaches.

Direct Ice Sensing

Direct ice sensing means that the sensor comes directly into contact with the accreted ice. Specific interactions between the sensor and the ice can be used to obtain information about the ice.

Capacitive Measurement

One direct approach for ice sensing is capacitive sensing [5, 7]. Figure 1.3 illustrates the principle of a capacitive ice sensor.

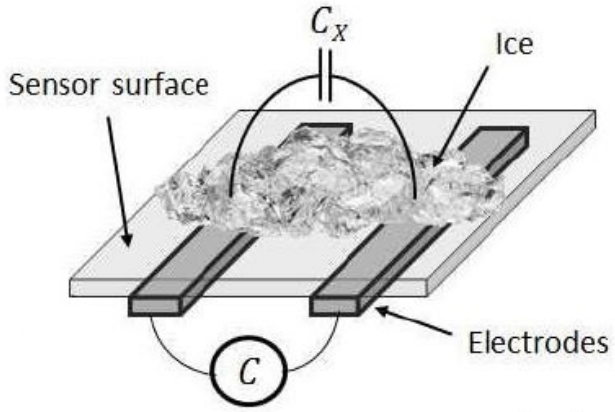

Figure 1.3: Illustration of a capacitive ice sensor. Accreted ice on the sensor surface changes the measurement capacitance C_x between the electrodes [5].

For this method the ice thickness is measured by the change of the capacitance. This change is caused by the relative permittivity of the accreted ice at a certain frequency. At the Institute of Electrical Measurement and Measurement Signal Processing (EMT) at Graz University of Technology a capacitive ice sensor has already been developed. In [8] the measurement principle is demonstrated and in [5] an uncertainty investigation regarding the estimation of the ice thickness is presented.

Impedance Measurement

A further direct sensing principle is based on the measurement of the complex dielectric material properties of ice over a certain frequency range. This can also be used to improve the detection of water and ice, as permittivity and conductivity are different for the two materials [9]. In [10], a sensor architecture and a corresponding evaluation based on electrical impedance spectroscopy is presented.

Indirect Ice Sensing

Indirect ice sensing means that the sensing element does not interact directly with the accreted ice. Relevant information about the ice is obtained from indirect measurements/observations.

Vision-based Measurement

An approach to obtain information about the ice thickness on transmission lines is the usage of a camera-based measurement system, as presented in [11]. By means of image processing an automated measurement of the ice thickness can be obtained. However, it can be difficult to reliably detect ice as different weather events like fog or heavy rain influence the vision between transmission line and camera. Ambient light conditions will also affect reliability, thus proper illumination is necessary to provide enough light.

Force-based Measurement

A force-based method is a further indirect sensor principle to obtain information about the ice load on transmission lines. Additional ice mass on the lines changes the tension of the line. This change of the tension can be measured by force sensors, which are mounted at the insulator. However, other factors like wind, which also exerts the lines and changes the tension, have to be considered as well in order to make a qualitative statement regarding the ice thickness [12].

Optical Measurement

An optical approach of monitoring the ice thickness on a transmission line is Fibre Bragg Grating (FBG) [13]. This sensor uses specifically manufactured glass fibres, which are capable of reflecting a desired wavelength. The FBG sensor is mounted on the transmission line. It emits a signal along the fibre and tracks the shift of the wavelength of the reflected "Bragg" signal. The shift of the wavelength depends on the strain and temperature. Once ice is accreted on the transmission line, the strain of the line changes due to the additional mass of the ice and so does the wavelength. By means of the detected wavelength shift, a statement about the ice thickness is possible.

1.1 Natural Ice Accretion Process

Natural ice by itself is a medium, which is complicated to describe. Several impacts influence the ice accretion process and the resulting ice volume. Depending on the ambient temperature, wind and humidity, the accreted ice and the ice composition can differ significantly. In this section the random effects and variations, which can arise during an ice accretion process are pointed out.

A primary distinction for ice is given by the different types of ice. In [14], different types of ice are described. The type of ice mainly depends on the ambient temperature during the accretion process. The amount of trapped air inside the ice and the corresponding composition of the ice differs for each particular process of ice accretion.

A further explicit variation, which comes along with the natural ice accretion process, is the random surface of the ice. The surface of an accreted ice volume is never ideally flat. Due to several impacts, such as wind, the surface of the ice volume always looks different and the ice thickness varies locally. Besides the uneven surface, also the texture of the surface is different for every ice formation. Owing to the crystalline structure of the ice, the microscopic texture of the surface is rough [14].

Especially direct ice sensing principles have to cope with the random nature of the ice accretion process. An ideal ice sensor should be capable of detecting the ice and measuring the ice thickness properly, regardless of the specific ice growth.

A direct sensing principle, which has been reported to be capable of distinguishing between different types of ice, is fibre optical ice sensing.

1.2 Fibre Optical Ice Sensing

Besides FBG, a different approach of using glass fibres for a possible ice sensor leads to the so-called Fibre Optical Ice Sensor (FOIS). Several recent publications address the FOIS sensing principle [15–19]. In this section the principle of fibre optical ice sensing is briefly discussed. The following explanation of a possible FOIS, seen in Figure 1.4, is based on [15].

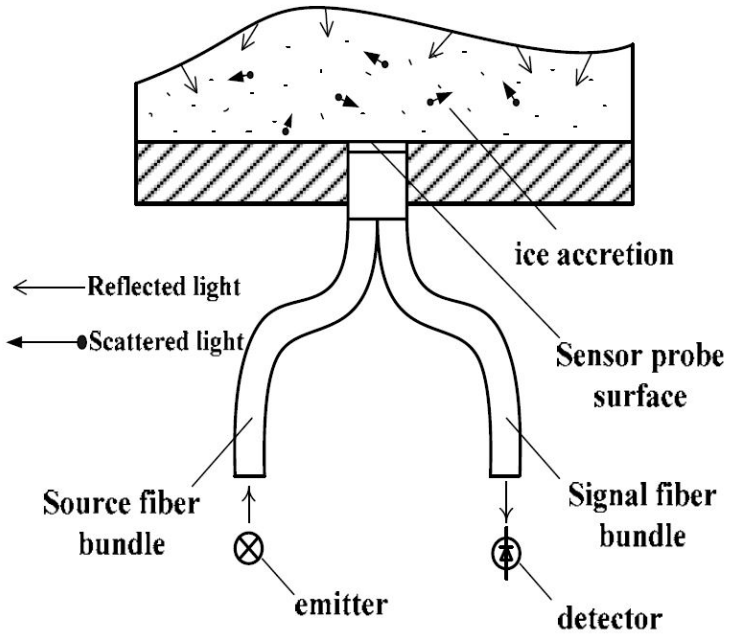

Figure 1.4: Structure of a possible FOIS. The emitted light is guided into the accreted ice, where it is reflected and scattered. The light seen on the sensor probe surface is forwarded to a detector [15].

A FOIS uses glass fibres in order to guide the emitter light into the ice volume and to forward reflected and scattered light towards the detector. The single glass fibres are bundled and form the source and signal fibre bundles. Both bundles are brought together at the sensor probe surface. The ice can grow on this surface.

The accreted ice volume is also depicted in Figure 1.4. As indicated, the incident light is reflected or scattered inside the volume. By the amount of light from the signal fibre bundle, it is possible to measure the ice thickness directly. The detector transforms the received light into an electric current, which can be processed to a proper voltage.

A typical sensor signal is depicted in Figure 1.5. It shows the voltage of the sensor signal as a function of the ice thickness. Different ice types are realized by maintaining different temperatures during the experiments.

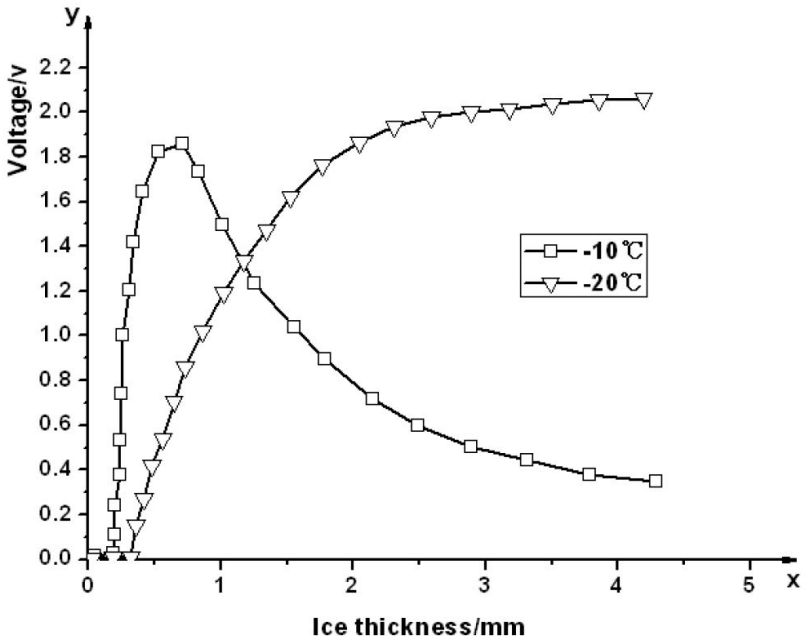

Figure 1.5: Characteristic voltage trends for a FOIS. For ambient temperatures around -10°C, the voltage first increases up to a certain maximum and drops with increasing ice thickness. At -20°C, the voltage steadily increases with increasing ice thickness [19].

The experimental results show that there is a significant difference for accreted ice at -10°C and -20°C. The two different voltage curves can be related to the ice type. Due to the structure of this sensor and its sensing principle, it is sensitive to the inner composition of the ice volume, and therefore the capability of determining the ice type is inherently included.

In [15], a first approach describes the relation between the intensity of detected light and the ice thickness in a mathematical way. The derivation is based on the geometry of the sensor and the ice. Other publications show experimental results for different sensor structures.

Fibre optical ice sensing is a direct approach to obtain information about the state of the ice. The interference between sensor and the random nature of the ice accretion process is a critical factor, which has to be addressed in order to characterize the capabilities of detecting ice and measuring the ice thickness.

1.3 Thesis Outline

This section provides an overview of the chapters in this thesis. Each chapter and the associated work is described.

Chapter 2 provides a review of the FOIS. The basic sensing principle is explained by describing the interaction between the incident light and the accreted ice. Furthermore, the already mentioned ice types are explained in a more detailed way. The last part of this chapter provides a table of related works. The different published works are compared to each other in terms of the requirements for an ice sensor.

A simulation framework for a FOIS is set up in Chapter 3. The simulation is based on a "Ray-Tracer". All required optical laws for the simulation are described. Furthermore, an overview of the used radiometric quantities is given. The direction and radiant flux of the rays, as they propagate through fibres and ice, are described as well. It is presented, which interfaces have to be considered and which effects happen at each point. A sensor model, based on a related work, is set up, and the relevant derivations for the model are shown.

In Chapter 4, the construction of a FOIS is presented. The mechanical construction of the entire sensor is depicted and described step by step. Furthermore, the required electronic components are introduced, and it is demonstrated how they can be optically coupled to the fibre bundles.

Chapter 5, the constructed sensors are used for different measurement experiments in a climatic chamber. First of all, the measurement setup is described. Measurement experiments for two distinct ice types are performed. The realization of each ice type is depicted and the corresponding trend of the sensor signal is provided. Furthermore, the cross sensitivity with respect to water is investigated. Additionally, simulations are performed in order to compare them with the measurement results. By means of the sensor model, a Monte Carlo Analysis for one ice type is carried out. The simulation includes the random effects during ice accretion. For each simulation, a random surface is generated and also the structure of the ice volume is composed in a random way. The results of this simulation are used to compute the Cramer-Rao lower bound (CRLB) for the FOIS in order to determine the uncertainty of the ice thickness measurement.

2 Review of Fibre Optical Ice Sensing

This chapter provides a description of the basic sensing principle used for a FOIS. The sensor effect is explained by means of the interaction between incident light and accreted ice. Additionally, different ice types and their impact on the sensor are described. Furthermore, an overview of different FOIS realizations is given. The most important parameters of the sensor are reviewed.

2.1 Basic Sensing Principle of the FOIS

In this section, the propagation of the incident light into the ice is discussed. It is shown how the interaction between light and ice can be used to measure the ice thickness. In Figure 1.4, a possible arrangement of a FOIS is sketched. A FOIS consists of a light emitting element, which is required to generate the necessary incident light. Figure 2.1 illustrates the propagation of the incident light, labelled by I_0, into the ice volume.

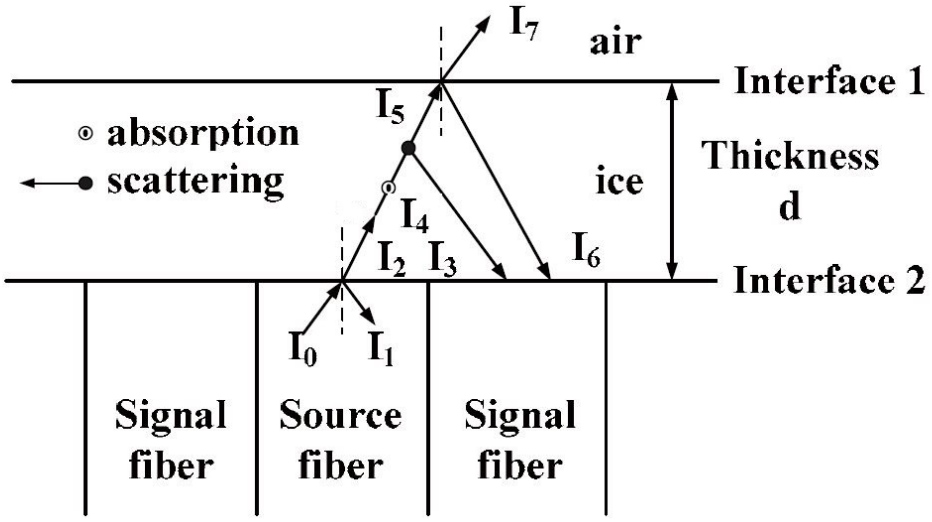

Figure 2.1: Propagation of light into the ice volume. The incoming light is either absorbed, scattered or reflected inside the ice volume or the boundaries [15].

At Interface 2 (fibre/ice) a portion of I_1 is reflected back into the source fibre. I_2 enters the ice and is

- absorbed (I_4),
- scattered (I_3) and
- reflected (I_6) at Interface 1 (ice/air).

Hence the light received at the detector is due to I_3 and I_6. I_7 is the amount of light propagating into the air. This fraction of the light cannot be detected any more. The amount of detectable light depends on the accreted ice thickness d and is the sum of reflected and scattered light falling onto the signal fibre.

In [15], a mathematical description is presented, which shows how the intensity of detected light is related to the ice thickness. This derivation is based on three assumptions:

1. The ice is ideally transparent.
2. The scattered light is neglected, because the ice is totally clear.
3. The surface of the ice is completely flat.

If the assumptions mentioned above hold, the propagation of the incident light into the ice is represented by a symmetrical cone with a divergence angle θ_d. This angle depends on the material property of the fibre [15]. The propagation of the incident light is illustrated in Figure 2.2.

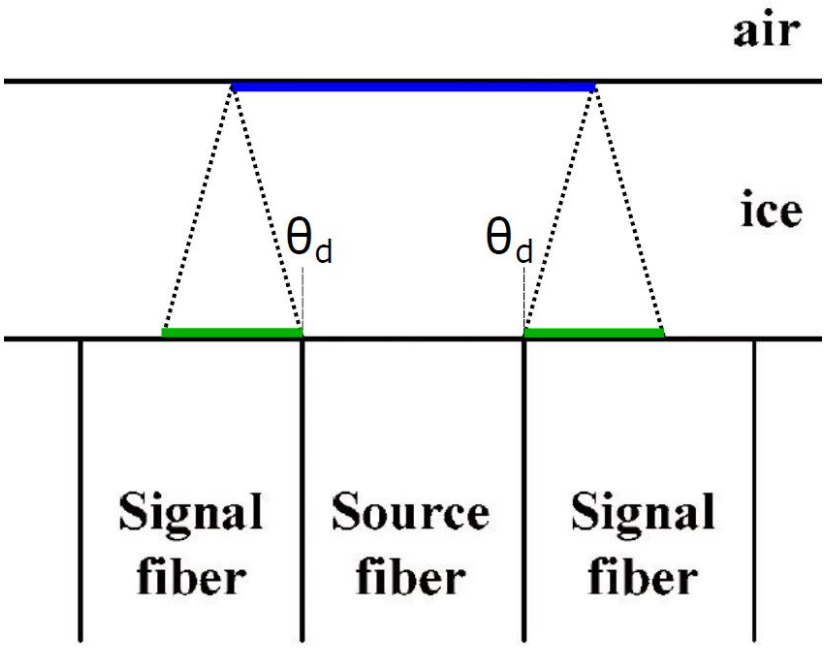

Figure 2.2: The incident light is represented by a symmetrical cone. Its image is projected onto the ice/air interface. The image (blue) is then reflected by the interface and its reflection (green) is seen on the signal fibres.

The image (blue) of the source fibre is projected onto the ice/air interface. Due to the flat surface it is ideally reflected. The reflection (green) is seen on the surrounding signal fibres.

The top view of this arrangement is depicted in Figure 2.3. For simplicity, only the right-hand signal fibre is considered.

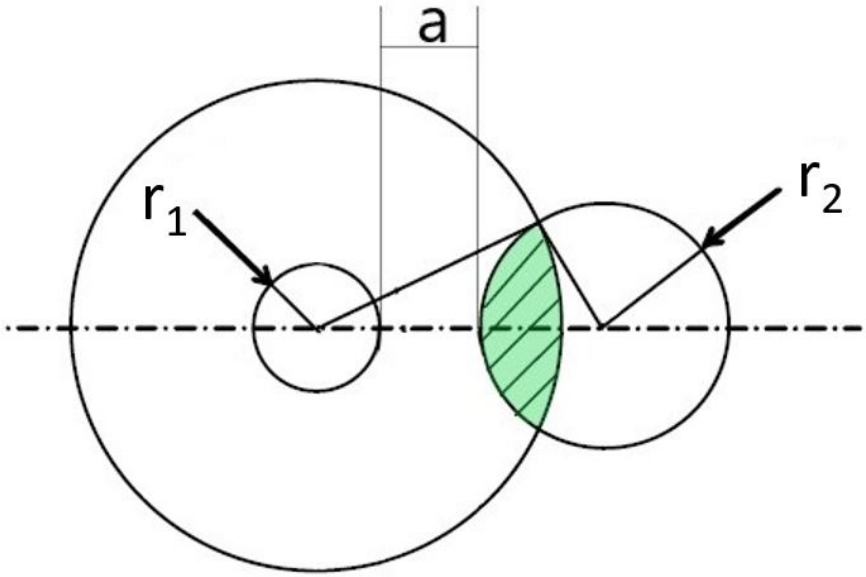

Figure 2.3: Overlap of the reflection and signal fibre area. As the ice thickness increases, the green area increases as well, until the signal fibre is completely covered. a denotes the distance between the source and the signal fibre [15].

The area of the source fibre is a circle with radius r_1. The area of the signal fibre is a circle with radius r_2. Due to the assumption of clear ice, the image of the source fibre is a circle as well. This image is projected onto the ice/air interface and is then ideally reflected onto the area of the signal fibre, leading to an overlap (green area) of two circles. This area represents the illuminated part of the signal fibre. As the ice thickness increases, the ice/air interface retreats away and the reflection of the incident light moves over the signal fibre until its surface is completely covered. For a certain thickness range, the resulting intensity seen on the signal fibre is described by the overlapping area marked in green.

The corresponding intensity is illustrated in Figure 2.4. For increasing ice thickness, the intensity increases as well. A maximum value is achieved when the signal fibre is completely covered. Due to absorption, the intensity is decreased. Additionally, the impact of distance a on the result is also shown.

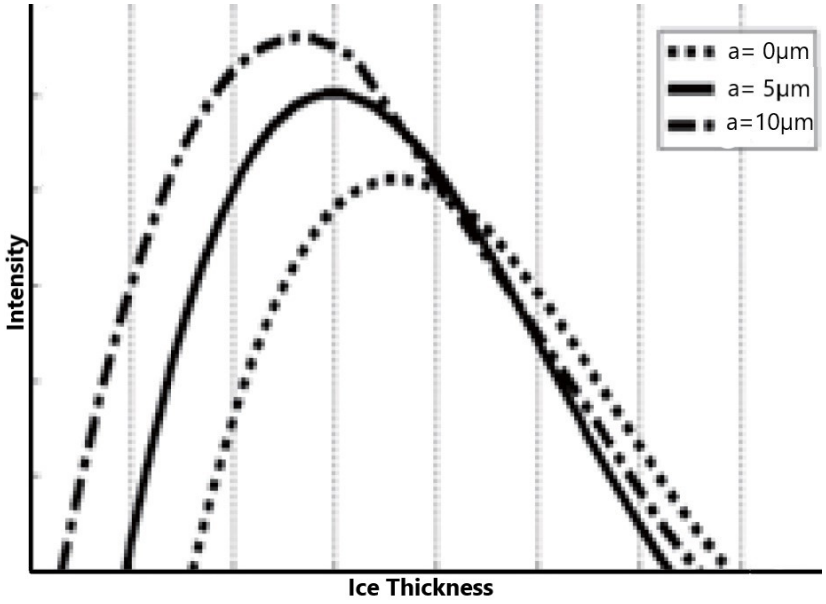

Figure 2.4: Trend of the intensity as a function of the ice thickness. For increasing ice thickness, the intensity increases as well, peaking at a certain thickness. Due to absorption, the intensity decreases again [15].

The approach presented in [15] is often used to describe the sensor effect and provides a model for the sensor signal. However, the model does not consider

- any impurities, e.g. trapped air, inside the ice volume,
- the uneven ice surface and
- different types of ice.

Therefore it might not be sufficient. As indicated in Figure 2.1, scattered light can also contribute to the illumination of the signal fibre.

2.1.1 Ice Types

The signal characteristics of the sensor depend on the ice type. Generally, one can distinguish between three different types of ice.

The first ice type is called "Glazed Ice". It is formed at ambient temperatures of around -5°C. Glazed ice is seen as very clear ice. Due to the low temperature the ice forms very slowly, which means that the amount of air traps (cracks and micro bubbles) is low inside the ice volume. This is why it is transparent.

The second type of ice is called "Rime Ice". At ambient temperatures of about -20°C the ice accretion process is faster than for glazed ice, thus more air is trapped in the ice, leading to an increased number of cracks and bubbles. Due to this high amount of air in the ice, every wavelength is scattered and the ice is no longer optical transparent.

The third type refers to so-called "Mixed Ice". It grows when the ambient temperature is about -10°C to -15°C. It contains more air compared to glazed ice. The transparency is slightly better than the transparency of rime ice.

Depending on the ice type, either the reflected or the scattered light is mainly responsible for the sensor output. For glazed ice, the scattered light has less impact on the output. As the number of cracks and bubbles is low, the light is not affected by significant scattering and the reflection dominates.

For rime ice, the impact of the reflection is smaller compared to the scattered light. The high amount of cracks and bubbles leads to a dominant scattering of the light. Hardly any light is seen on the ice/air interface and therefore the influence of the reflection is lower.

2.2 Overview of FOIS

Figure 2.5 gives an overview of published related works regarding FOIS. The capability of detecting early ice accretion and a measurement for the ice thickness are the most important parameters regarding ice sensors.

Author	Title	Sensor Characterization							Sensor Bundle
		Detection	Thickness	Accretion Rate	Ice Type	Hardware (Ice Sensor)	Range in mm	Wave length in nm	
Wei Li, Jie Zhang, Lin Ye [15]	Modelling and Experimental Study on the Fiber-Optic Ice Sensor	Yes Shows that a minimum thickness is necessary	Yes Shows influence of arrangement	Yes	No Simplified Model, Assume glazed Ice only	Not specified (Model with 2 fibre)	7	n/a	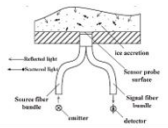
Wei Li, Jie Zhang, Lin Ye [19]	A Fiber-Optic Solution to Aircraft Icing Detection and Measurement Problem	Yes	Yes	Yes	Yes (but a certain thickness is necessary to clearly distinguish between types)	Not specified bifurcate fibre bundle (Only system block diagram)	4.5	n/a	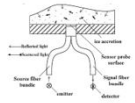
Junfeng Ge, Lin Ye, Jianhong Zou [16]	A novel fiber-optic ice sensor capable of identifying ice type accurately	Yes	Yes	Yes	Yes (A dedicated sensor for ice type identification)	Custom Bundle divided in 3 parts	10	940	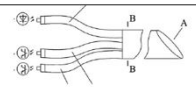
Jianhong Zou , Lin Ye, Junfeng Ge, Chengrui Zhao [18]	Novel fiber optic sensor for ice type detection	Yes	Yes	Yes	Yes (A dedicated sensor for ice type identification)	Sensor is split into 3 parts. Oblique source bundle and oblique signal bundles	10	940	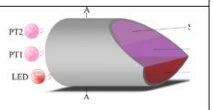
Jianhong Zou, Lin Ye and Junfeng Ge [17]	Ice type detection using an oblique end-face fibre-optic technique	Yes	Yes	Yes	Yes (A dedicated sensor for ice type identification)	Sensor is split into 4 parts. 2 source bundles, 2 signal bundles Double effort	10	935	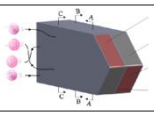

Figure 2.5: Overview of Fibre Optical Ice Sensors. The capabilities for ice detection and for thickness measurement is stated for all listed sensors. Furthermore, the ice type can be determined by three dedicated sensor structures.

It can be seen that all of the listed sensors are capable of detecting the beginning of the ice formation. Furthermore, the ice thickness and the accretion rate over time can also be determined with these sensors. One additional feature, which is also listed, is the capability to determine the ice type, as explained in Section 2.1.1. There are dedicated sensors, which provide information about the ice type as well.

Furthermore, the required hardware and the structure of the sensor is depicted. It can be seen that the structure of a FOIS is always similar. A source fibre or source bundle is required to couple light into the ice volume. The source for the input light is typically a Light-Emitting-Diode (LED) with a certain wavelength λ. At least one signal fibre or signal bundle is needed to collect the incoming light from the ice volume, before a photosensitive element converts the detected light into a proper photo-current.

To clearly distinguish between different types of ice and to avoid the impact of the ambient light, the effort in terms of hardware is increasing. The sensor bundle becomes more complex and also the electronic complexity of the circuits increases. In [19], the use of modulated light in combination with a lock-in amplifier is presented. In [16], a differential evaluation is carried out using an electronic circuit.

The listed publications show experimental results with their different sensor structures. However, while ice sensing is referred to as a direct sensing principle, the sensing effect is of non-linear nature. Furthermore, the random nature of the ice accretion process has to be described properly in order to address the capabilities regarding detection and thickness measurement. In the upcoming chapter a simulation framework is set up. It is used to describe the interaction of the sensor with the ice including its random accretion process.

3 Simulation Framework for FOIS

This chapter presents the modelling and simulation of the sensor. The assumptions addressed in Section 2.1 are extended by spatial effects for the light propagation during the ice accretion including

- scattering events and
- diffuse reflection at an uneven surface.

For a description of the natural behaviour of light and its propagation in the ice volume, fundamental optical laws are required. One could consider light as electromagnetic wave. The wave behaviour can then be described by solving the Maxwell Equations. However, a more convenient implementation of the optical laws is provided by geometrical optics. For this approach the propagation of light is modelled by means of so-called "rays". A ray is defined as a drawn line in space, representing the direction of flow of radiant energy. The rays are perpendicular with respect to the wave fronts [20]. The description of the rays including all relevant radiometric quantities and optical laws is brought together in a so-called "Ray-Tracer". By means of this simulation, one can obtain a better understanding of the resulting sensor output and which effects are present during ice accretion.

The amount of emitted and detected light has to be described in terms of radiometric quantities. Table 3.1 lists the radiometric quantities, which are used in the further discussion.

Name	**Definition**	**Unit**	**Description**
Radiant Energy	Q_e	J	Energy of electromagnetic radiation
Radiant Flux	$\Phi_e = \frac{\partial Q_e}{\partial t}$	W	Radiant Energy per time unit
Irradiance	$E_e = \frac{\partial \Phi_e}{\partial A}$	$\frac{\mathrm{W}}{\mathrm{m}^2}$	Radiant Flux per unit area

Table 3.1: Overview of Radiometric Quantities used in Ray-Tracer.

3.1 Effects for Sensor Modelling

In this section all of the relevant optical laws are explained. Figure 3.1 depicts the propagation of a ray from a fibre within the source bundle to the signal bundles as it will be used in the model. On the basis of this illustration the relevant optical laws are described.

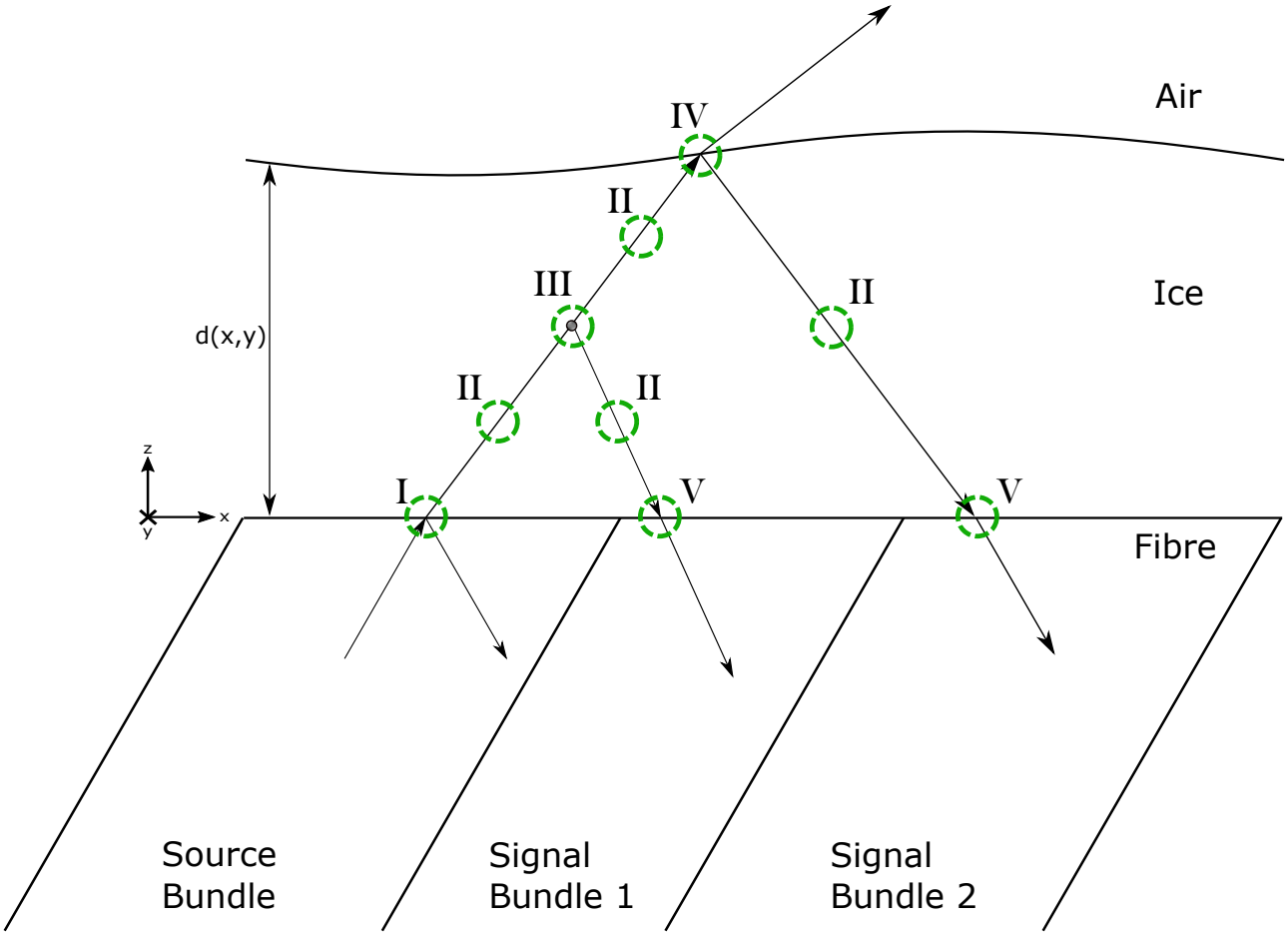

Figure 3.1: Coupling from the source into signal bundles. At **I** the light reaches the fibre/ice interface. At **II** the absorption effect is present. **III** is a point where the light is scattered by a potential air bubble. The ice/air interface is at **IV**. The coupling from ice to fibre glass is shown at point **V**.

I : Fibre/Ice Interface

At this interface the incoming light from the source bundle is coupled into the ice volume. To fully describe all effects which have to be considered at this point, some optical quantities and laws regarding the properties of the material have to be defined.

3.1.1 Refractive Index

The absolute index of refraction n is defined as

$$n = \frac{c}{v}, \tag{3.1}$$

where c denotes the velocity of light in vacuum, and v denotes the velocity of light in a specific material.

For glass fibre cores n_{Fibre} is 1.581. The refractive index of ice n_{Ice} is 1.31 [20].

Once the refractive index of the relevant materials is known, the direction of the ray transmitted into ice and the ray reflected back into the source bundle has to be determined. This can be done applying the laws described in Section 3.1.2 and Section 3.1.3.

Essential for the FOIS is also the computation of the radiant flux at an interface. This derivation is shown in Section 3.1.4.

3.1.2 Law of Reflection

This law describes in which direction an incident ray is reflected when it reaches an interface. This is depicted in Figure 3.2. For the definition of this law, two angles have to be introduced. Both the angle of incidence θ_{i} and the angle of reflection θ_{r} are measured from a perpendicular drawn to the reflecting surface. The Law of Reflection states that the angle of incidence equals the angle of reflection

$$\theta_{\text{i}} = \theta_{\text{r}}. \tag{3.2}$$

Equation (3.2) is valid when the incident ray, the perpendicular to the surface and the reflected ray are within the plane of incidence [20].

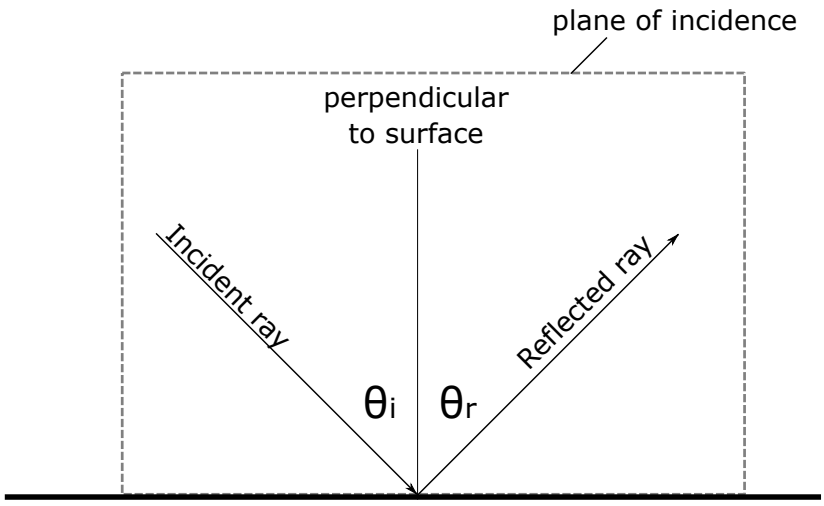

Figure 3.2: An incident ray reaches a surface and is reflected. The Law of Reflection states that the incident angle θ_i equals the the reflection angle θ_r. Both rays and the perpendicular are within the plane of incidence.

Specular versus Diffuse Reflection

If the deformations on the surface are small compared to wavelength λ, the surface is defined as flat. The process, when all reflected rays at the flat surface merge and form a defined beam, is called specular reflection [20]. Figure 3.3 illustrates the case of a specular reflection.

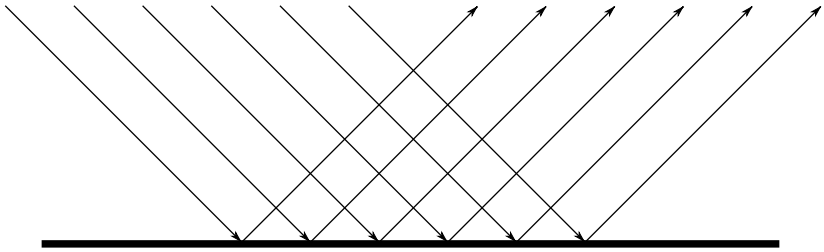

Figure 3.3: A specular reflection occurs when the wavelength λ of the incident light is large compared to the dimensions of deformations on the surface.

Once the wavelength λ is smaller compared to the surface deformation, the surface is considered as rough and the specular reflection vanishes. In this case Equation (3.2) is still valid for every single ray. However, the reflected rays do not form a defined beam any more. This process is referred to as diffuse reflection.

Normally the ice surface is rough, meaning that no specular reflection occurs. Most of the time the diffuse reflection is dominant, which is pictured in Figure 3.4.

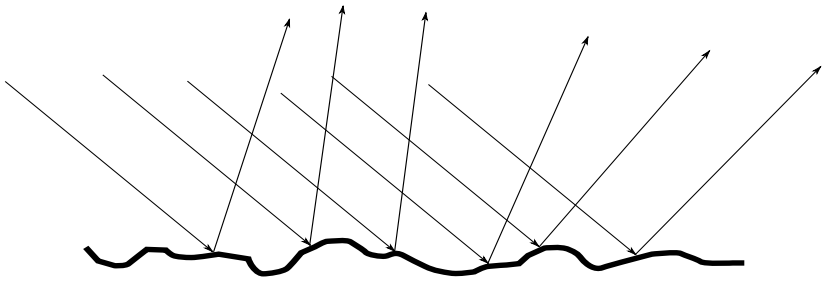

Figure 3.4: Diffuse reflection occurs when the wavelength λ is smaller compared to the dimensions of the deviations on the surface.

3.1.3 Law of Refraction

The Law of Refraction describes the relation between the incident ray and the transmitted or refracted ray regarding their angles to the perpendicular when a ray passes through an interface. Figure 3.5 shows the graphical representation.

The Law of Refraction states that

$$n_{\mathrm{i}} \sin(\theta_{\mathrm{i}}) = n_{\mathrm{t}} \sin(\theta_{\mathrm{t}}). \tag{3.3}$$

Equation (3.3) is also called Snell's Law. n_{i} denotes the refractive index of the material in which the incident light propagates. The refractive index of the material where the refracted light is transmitted is labelled as n_{t}. θ_{i} labels the angle of the incident ray, and θ_{t} labels the angle of the transmitted ray. Both angles are measured from the perpendicular to the surface.

If the ratio $\frac{n_{\mathrm{i}}}{n_{\mathrm{t}}} < 1$, the transmitted beam is refracted towards the perpendicular. $\frac{n_{\mathrm{i}}}{n_{\mathrm{t}}} > 1$ leads to a refraction away from the perpendicular.

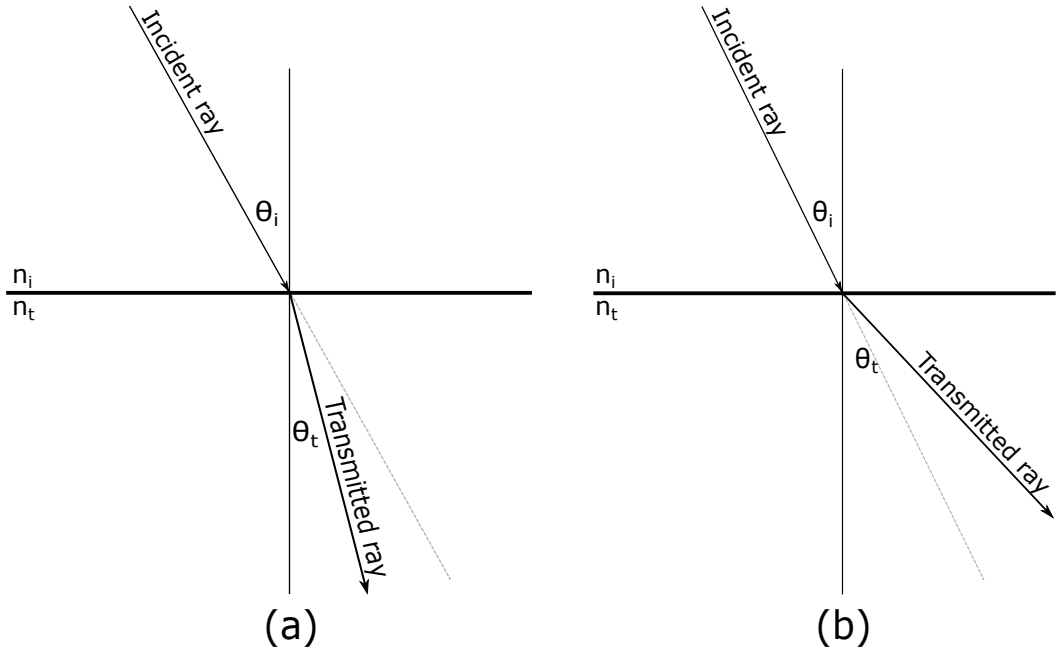

Figure 3.5: Law of Refraction: (a) depicts the case of $\frac{n_i}{n_t} < 1$. As a result the transmitted ray is closer to the perpendicular. (b) shows the case of $\frac{n_i}{n_t} > 1$. The transmitted ray is further away from the perpendicular.

3.1.4 Fresnel Equations

By implementing the Law of Reflection and the Law of Refraction, the directions of the reflected light and the transmitted light are obtained. The next step is to compute the corresponding power of the reflected and the transmitted light at the interface. This is done by means of the Fresnel Equations. In order to define them, the incident wave has to be seen as electromagnetic wave. It is then described by its electric field and its magnetic field. Both fields are represented as waves with a certain amplitude. For the Fresnel Equations, two cases regarding the electric field have to be considered [20]:

- Case 1: Incident wave is perpendicular to the plane of incidence.
- Case 2: Incident wave is parallel to the plane of incidence.

For the first case the following two equations are given:

$$r_{\perp} = \frac{E_{0\mathrm{r}}}{E_{0\mathrm{i}}} = \frac{n_{\mathrm{i}}\cos(\theta_{\mathrm{i}}) - n_{\mathrm{t}}\cos(\theta_{\mathrm{t}})}{n_{\mathrm{i}}\cos(\theta_{\mathrm{i}}) + n_{\mathrm{t}}\cos(\theta_{\mathrm{t}})} \tag{3.4}$$

$$t_{\perp} = \frac{E_{0\mathrm{t}}}{E_{0\mathrm{i}}} = \frac{2n_{\mathrm{i}}\cos(\theta_{\mathrm{i}})}{n_{\mathrm{i}}\cos(\theta_{\mathrm{i}}) + n_{\mathrm{t}}\cos(\theta_{\mathrm{t}})} \tag{3.5}$$

For the second case where, the incident wave is parallel to the plane of incidence, another two equations can be obtained:

$$r_{\parallel} = \frac{n_{\mathrm{t}}\cos(\theta_{\mathrm{i}}) - n_{\mathrm{i}}\cos(\theta_{\mathrm{t}})}{n_{\mathrm{i}}\cos(\theta_{\mathrm{t}}) + n_{\mathrm{t}}\cos(\theta_{\mathrm{i}})} \tag{3.6}$$

$$t_{\parallel} = \frac{2n_{\mathrm{i}}\cos(\theta_{\mathrm{i}})}{n_{\mathrm{i}}\cos(\theta_{\mathrm{t}}) + n_{\mathrm{t}}\cos(\theta_{\mathrm{i}})} \tag{3.7}$$

$r_{\perp}$, $r_{\parallel}$ are the so-called amplitude reflection coefficients, and $t_{\perp}$, $t_{\parallel}$ denote the amplitude transmission coefficients. $E_{0\mathrm{t}}$ labels the amplitude of the transmitted E-Field, $E_{0\mathrm{r}}$ labels the amplitude of the reflected E-Field, and $E_{0\mathrm{i}}$ denotes the amplitude of the incident E-Field.

The equations shown in Equation (3.4) to Equation (3.7) are called Fresnel Equations and give a relationship between the refraction indices, the angle of incident, the angle of transmittance and the amplitudes when light reaches an interface.

The dependency between the amplitude coefficients and the incident angle at a fibre/air interface is depicted in Figure 3.6. It can be seen that the amplitude coefficients increase with increasing incident angle until $\theta_{\mathrm{i}} \approx 39°$.

Reflectance and Transmittance

By means of the Fresnel Equations, a relation between the input power, the reflected power and the transmitted power can be obtained.

The reflectance R is the ratio of the reflected power to the incident power. The reflectance for the two cases is defined as

$$R_{\perp} = \frac{E_{0\mathrm{r}}^2}{E_{0\mathrm{i}}^2} = r_{\perp}^2 \tag{3.8}$$

and

$$R_{\parallel} = \frac{E_{0\mathrm{r}}^2}{E_{0\mathrm{i}}^2} = r_{\parallel}^2. \tag{3.9}$$

The transmittance T is the ratio of transmitted power and incident power. It can be computed as

$$T_\perp = \frac{n_\mathrm{t}\cos(\theta_\mathrm{t})}{n_\mathrm{i}\cos(\theta_\mathrm{i})}\frac{E_{0\mathrm{t}}^2}{E_{0\mathrm{i}}^2} = \frac{n_\mathrm{t}\cos(\theta_\mathrm{t})}{n_\mathrm{i}\cos(\theta_\mathrm{i})}t_\perp^2 \tag{3.10}$$

and

$$T_\parallel = \frac{n_\mathrm{t}\cos(\theta_\mathrm{t})}{n_\mathrm{i}\cos(\theta_\mathrm{i})}\frac{E_{0\mathrm{t}}^2}{E_{0\mathrm{i}}^2} = \frac{n_\mathrm{t}\cos(\theta_\mathrm{t})}{n_\mathrm{i}\cos(\theta_\mathrm{i})}t_\parallel^2. \tag{3.11}$$

The defined reflectance and transmittance of Equation (3.8) to Equation (3.11) can be used to define the overall reflectance by

$$R = \frac{1}{2}(R_\parallel + R_\perp). \tag{3.12}$$

Equation (3.12) is valid for natural light, which is considered not to have any polarization.

A further relation between reflectance and transmittance is

$$R + T = 1. \tag{3.13}$$

The corresponding reflectance and transmittance at a fibre/air interface is pictured in Figure 3.7. At an incident angle of $\theta_\mathrm{i} \approx 39°$ the reflectance approaches the value 1. According to equation (3.13) the transmittance becomes 0. This is referred to as Total Internal Reflection, which is explained in Section 3.1.5.

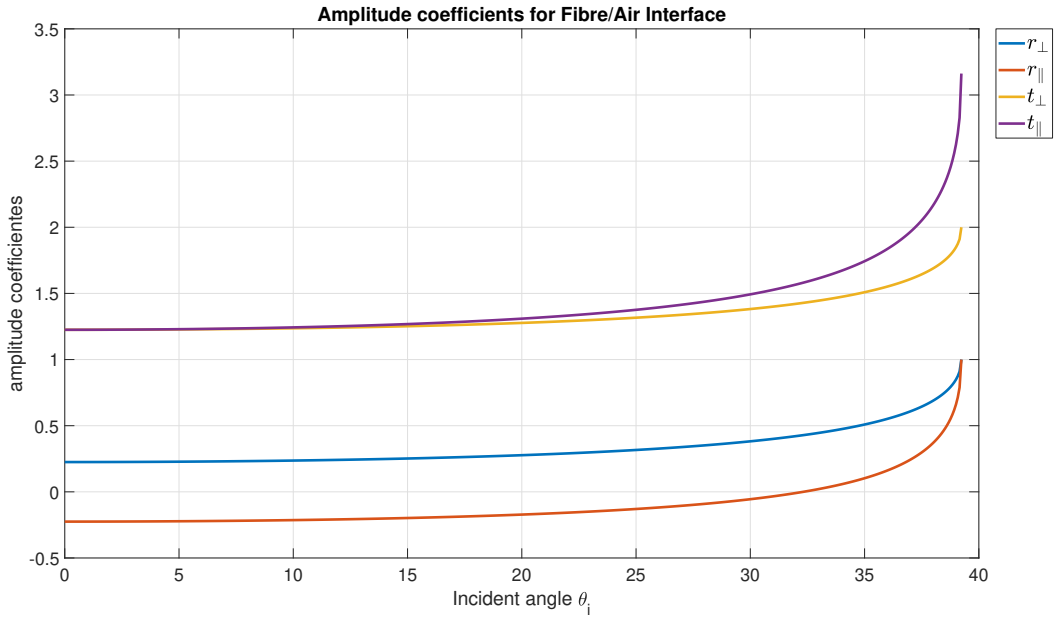

Figure 3.6: Amplitude coefficients for fibre/air interface as a function of the incident angle θ_i.

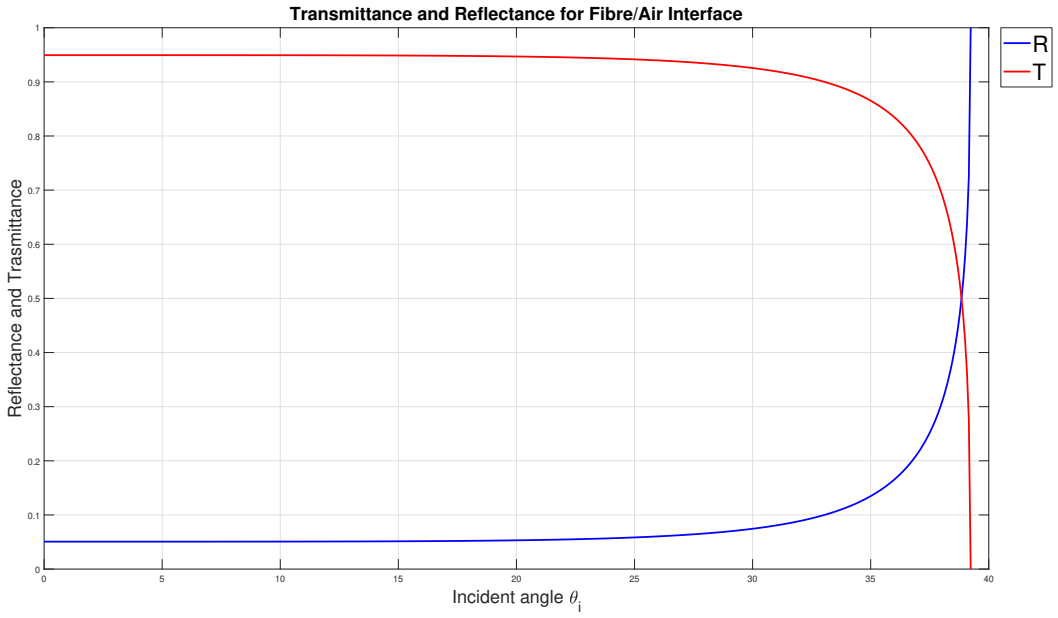

Figure 3.7: Reflectance and transmittance for fibre/air interface as a function of the incident angle θ_i.

3.1.5 Total Internal Reflection

The assumption that the incident ray is split up into the reflected ray and the transmitted ray is not always valid. The case of an internal reflection is given when $n_\mathrm{i} > n_\mathrm{t}$ holds. In this case the refraction angle increases for increasing incident angle, as indicated in Figure 3.5 (b). Figure 3.7 shows that with increasing incident angle the reflectance R approaches the value 1 at a certain incident angle. At this critical point $\theta_\mathrm{t} = 90°$ and $\theta_\mathrm{i} = \theta_\mathrm{c}$. θ_c denotes the critical angle and it is calculated by

$$\theta_\mathrm{c} = \arcsin\left(\frac{n_\mathrm{t}}{n_\mathrm{i}}\right). \tag{3.14}$$

Once $\theta_\mathrm{i} \geq \theta_\mathrm{c}$, no light is transmitted any more through the interface, leading to a Total Internal Reflection of the incident ray.

The process of a Total Internal Reflection is depicted in Figure 3.8, which considers a fibre/air interface. For $n_\mathrm{i} = n_\mathrm{Fibre} = 1.581$ and $n_\mathrm{t} = n_\mathrm{Air} = 1$, the corresponding critical angle becomes $\theta_\mathrm{c} = 39.23°$.

At $\theta_\mathrm{i} = 15°$ the reflectance is 5 %, illustrated with a light gray arrow. At $\theta_\mathrm{i} = 37°$ the reflectance increases to 21.65 %. Once $\theta_\mathrm{i} \geq \theta_\mathrm{c}$, the reflectance increases up to 100 % and the transmitted ray disappears.

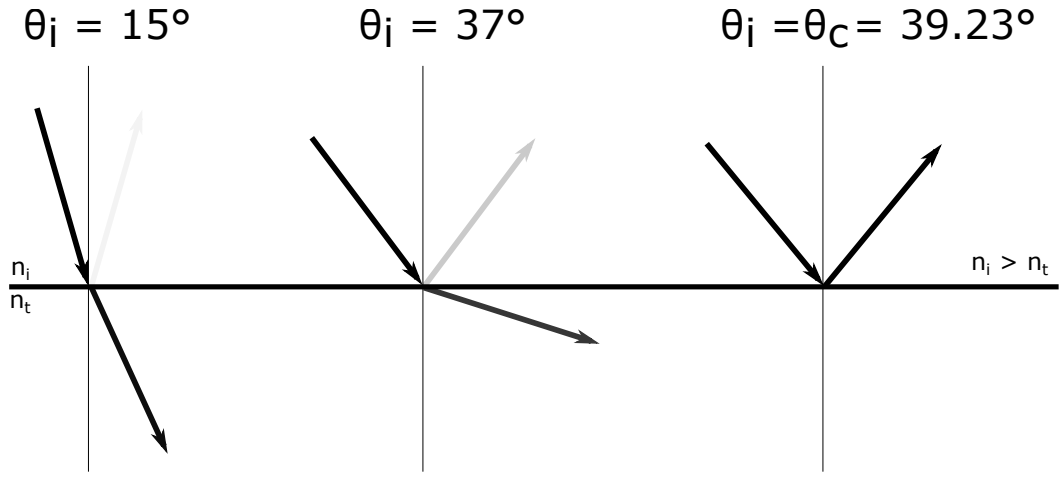

Figure 3.8: Total Internal Reflection for fibre/air interface. As the incident angle increases, the reflectance also increases. 100 % is reflected when $\theta_\mathrm{i} \geq \theta_\mathrm{c}$.

II: Absorption

Once the light has entered the ice volume it propagates forward. In the course of propagation a certain amount of radiant flux is lost. The amount of loss depends on the distance and the absorption coefficient.

3.1.6 Beer-Lambert Law

If a wave of a certain wavelength propagates through a medium, the atoms of the material are excited by the wave. Energy is absorbed by the material and converted into heat by the oscillating atoms.

The reduction of flux at a certain distance inside a material is described by

$$\Phi_{\mathrm{e}}^{\mathrm{t}} = \Phi_{\mathrm{e}}^{\mathrm{i}} \cdot e^{-\alpha \cdot x}. \tag{3.15}$$

Equation (3.15) shows Beer-Lambert's Law. $\Phi_{\mathrm{e}}^{\mathrm{i}}$ labels the input radiant flux. $\Phi_{\mathrm{e}}^{\mathrm{t}}$ is the flux at a certain distance x. α denotes the absorption coefficient in m^{-1}. Figure 3.9 shows the dependency between the absorption coefficient of ice and the wavelength of the incident light. The absorption coefficient holds for glazed and rime ice.

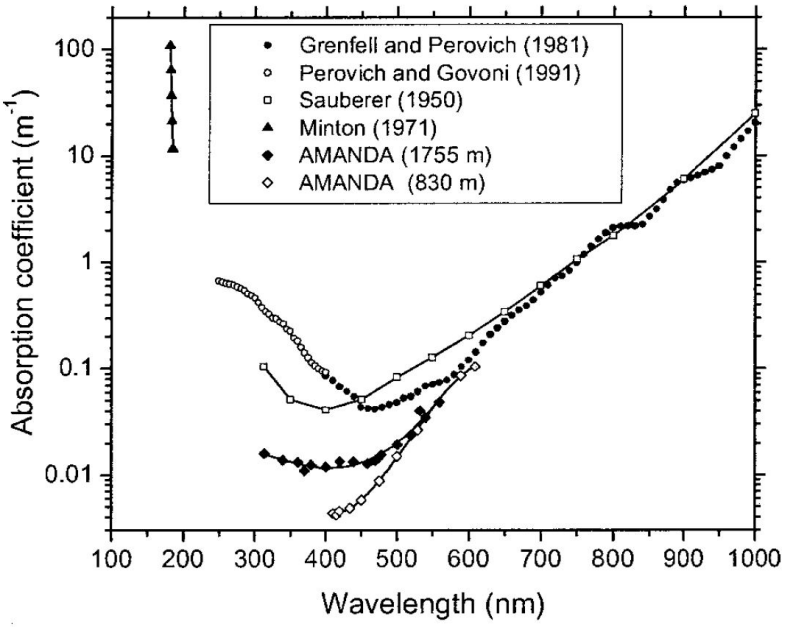

Figure 3.9: Absorption coefficient of ice as a function of the wavelength. Note that the absorption coefficient is plotted in logarithmic scale [21].

III: Cracks and Micro-Bubbles

This part discusses the scattering event, as a ray reaches a crack or a micro bubble. The influence of the objects onto the light is referred to as scattering. Generally, it can be distinguished between Rayleigh's Scattering and Mie Scattering. Which of these scattering patterns appears depends on the ratio of wavelength to the dimensions of the particle or the bubble. For Rayleigh Scattering the size of the scattering object has to be much smaller than the wavelength. Therefore, the scattering event of light in ice is described by Mie Scattering [14].

Mie Scattering

The Mie-Theory is an analytical solution of the Maxwell-Equations and describes the scattering of a plane electromagnetic wave by a homogeneous sphere, whose size is comparable or larger with respect to the wavelength of the wave.

The illustration of the scattering pattern with rays is depicted in Figure 3.10. In this figure, the lengths of the rays also represent the corresponding power of each ray. The incident ray is split up into many smaller rays. It can be seen that the rays with higher power point in a similar direction as the direction of the incident ray. Rays with less power are scattered all around the bubble.

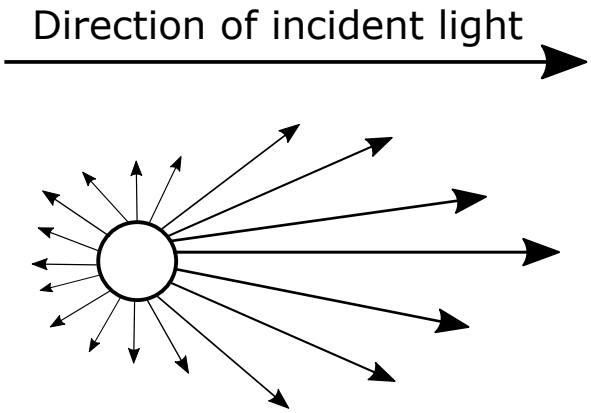

Figure 3.10: Process of incident light being scattered by a micro bubble. Once the wavelength of the light is comparable to the dimensions of the bubble, Mie-Scattering is a possible way to describe the pattern of the scattering.

For the simulation, an approximation of Mie-Scattering, as indicated in Figure 3.11, is implemented. The incident ray is split into two rays. The first one is forwarded without any change of the direction and represents the rays pointing in a similar direction as the incident ray. The second ray represents all the short rays around the bubble. In

the simulation this ray is deflected by a random angle θ_B.

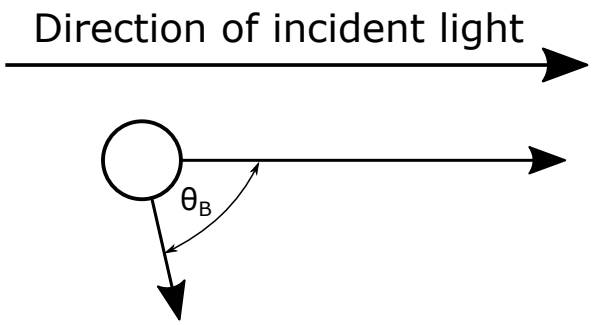

Figure 3.11: Approximated scattering pattern. The long ray has the same direction as the incident ray. The short ray is scattered by a random angle θ_B.

IV: Ice/Air Interface

Once the light passes the ice volume it reaches the ice/air interface, at which point a fraction of the light is reflected and the other fraction is transmitted into the air. The Law of Reflection and Refraction is reused and considers the refractive indices of ice and air. In air the refractive index $n_{\text{Air}} = 1.00028$ [20].

The Fresnel Equations are used to compute the amount of radiant flux for transmitted and reflected rays.

V: Ice/Fibre Interface

After the reflection of the ray at the ice/air interface, the light propagates towards the signal bundles. During this propagation its radiant flux is reduced by absorption again. The Law of Reflection and Refraction are now applied for the refractive indices for ice and fibre. The mechanism for the light coupling into a single fibre is described in the following section.

The amount of power, which is forwarded to the detectors, is computed by using the Fresnel Equations.

3.1.7 Fibre Optics

An important aspect of the sensor is the structure of a fibre itself. The FOIS consists of source fibres and signal fibres. The light inside the fibres does not propagate in a straight direction. It is reflected inside the fibre. The resulting angle of the emitted light occupies a defined range. The range of this angle is determined by the material of the fibres.

A glass fibre typically consists of a core coated by a cladding to minimize cross-talk between single fibres. The refractive index of the cladding n_c is smaller than the index of the core (fibre) n_f. Furthermore, the material at both ends of the fibre has to be considered. One end of the fibre (core+cladding) is placed in a medium, e.g. air, with refractive index n_i. The other end of the fibre could be in a different medium, e.g. ice, with refractive index n_t.

Figure 3.12 shows how an incident ray couples into a fibre and how the ray propagates forward. A ray with an incident angle θ_i reaches the surface of the fibre and is transmitted forward within the fibre with an angle of θ_t. For a successful transmission it is essential that the ray inside the fibre always performs a Total Internal Reflection when reaching a wall (fibre-cladding interface), otherwise the light cannot propagate.

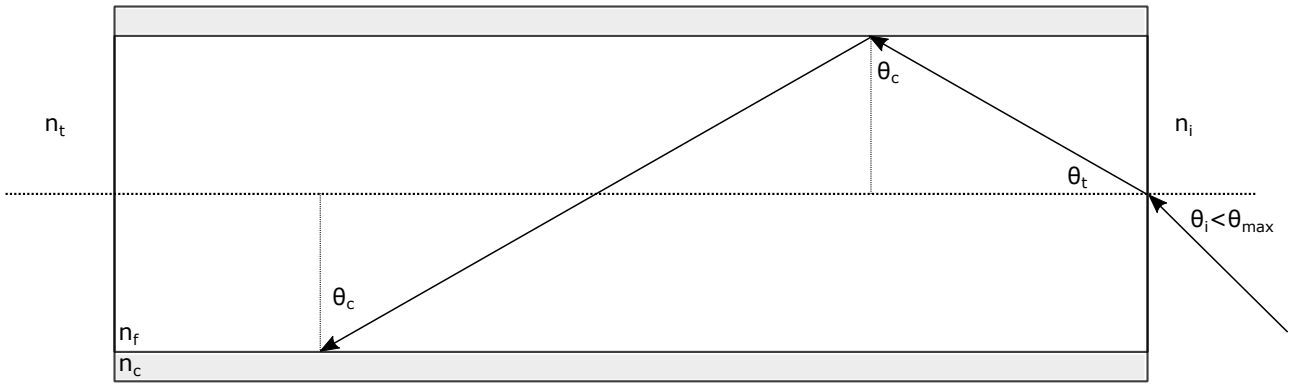

Figure 3.12: Structure of a glass fibre with an incident ray. The fibre core is illustrated in white, the cladding in gray. In order to achieve a desired Total Internal Reflection, the incident angle θ_i must not exceed θ_max.

In order to achieve a Total Internal Reflection, a certain maximum angle defined by

$$\sin\left(\theta_{\max}\right) = \frac{1}{n_{\mathrm{i}}}\sqrt{n_{\mathrm{f}}^2 - n_{\mathrm{c}}^2} \tag{3.16}$$

must not be exceeded at the input. Equation (3.16) shows that this maximum angle $\theta_{\max}$ depends on the materials of the fibre and on the refractive index n_{i}. If $\theta_{\mathrm{i}} > \theta_{\max}$, then the resulting angle at the fibre-cladding interface is smaller than the critical angle θ_{c}. The acceptance angle of the fibre is defined as $2\theta_{\max}$.

The product of $n_{\mathrm{i}} \cdot \sin\left(\theta_{\max}\right)$ is referred to as numerical aperture (NA). This number describes how much light can be collected by the fibre from a surrounding material. The NA has a value between 0 and 1, whereby 1 is only achievable in vacuum. A NA of 1 leads to $\theta_{\max} = 90°$. The corresponding acceptance angle of 180° means that all incident light on the surface is totally reflected inside the fibre [20].

For a FOIS, the NA of the glass fibre is a crucial parameter. It has to be chosen properly to ensure that most of the light is gathered by the signal fibres to achieve a convenient sensor signal.

3.2 Sensor Model and Simulation Steps

In this section, the model of the sensor is introduced and the steps, which need to be performed during the simulation, are explained.

The described laws regarding the light propagation and the power considerations are now brought together in the Ray-Tracer. The model, which is used in the Ray-Tracer, is applied for the sensor presented in [16]. The structure of this sensor consists of one source bundle and two signal bundles. The sensor has an inclination with an inclination angle $\theta_{\text{Incl}} = 30°$.

3.2.1 Sensor Model

The model is set up in MATLAB. The top view of the corresponding sensor area and the arrangement of the bundles is depicted in Figure 3.13. Due to the inclination, the sensor surface is of elliptic shape. The ellipse is approximated by means of two semicircles with radius R, representing the source bundle and signal bundle 2, and a rectangle with length B and width 2R, representing signal bundle 1.

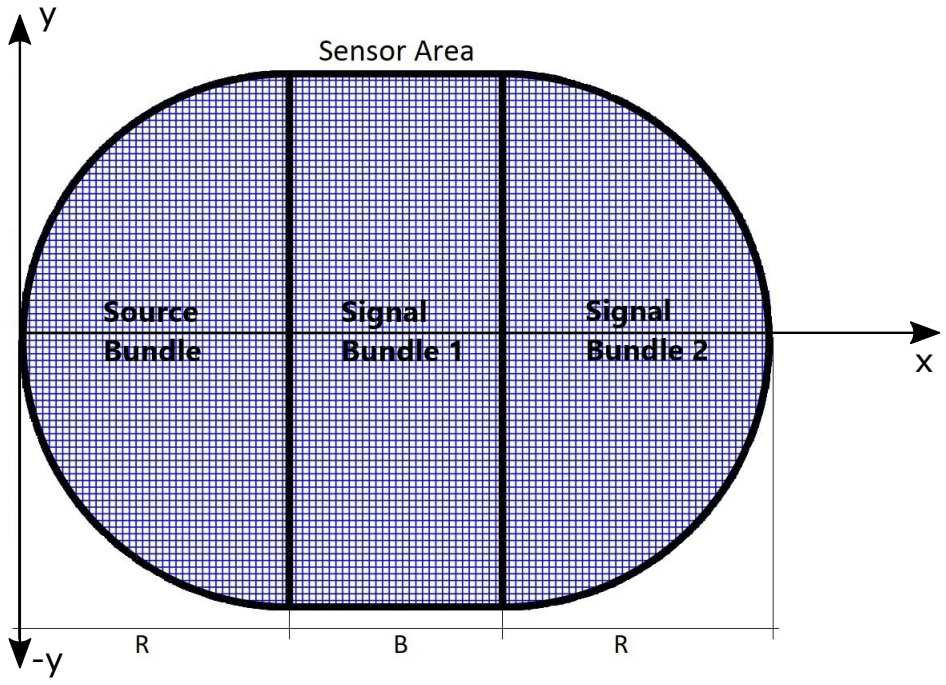

Figure 3.13: Top view of the sensor area. Due to the inclination, the surface is an ellipse. This is approximated by 2 semicircles with radius R and a rectangle with length B.

In order to locate the single fibres within the bundles, the area is quantized. The localization in x and y direction is implemented by means of a uniform grid. Each point in the grid represents one single fibre. Fibres within the signal bundles are defined as signal fibres. Fibres within the source bundle are defined as source fibres. Every source fibre emits one ray. For the description of the propagation in ice, each ray is assigned a

- certain initial radiant flux Φ_{Ray} and
- incident angle θ_{i}.

To illustrate the mode of operation, one single ray is described as it is emitted by a source fibre and propagating through the ice.

3.2.2 Derivation at Interfaces

The propagation of the single rays and their radiant flux have to be described for each interface properly in order to model all the relevant effects. Figure 3.14 shows an exemplary ray propagating through the ice volume.

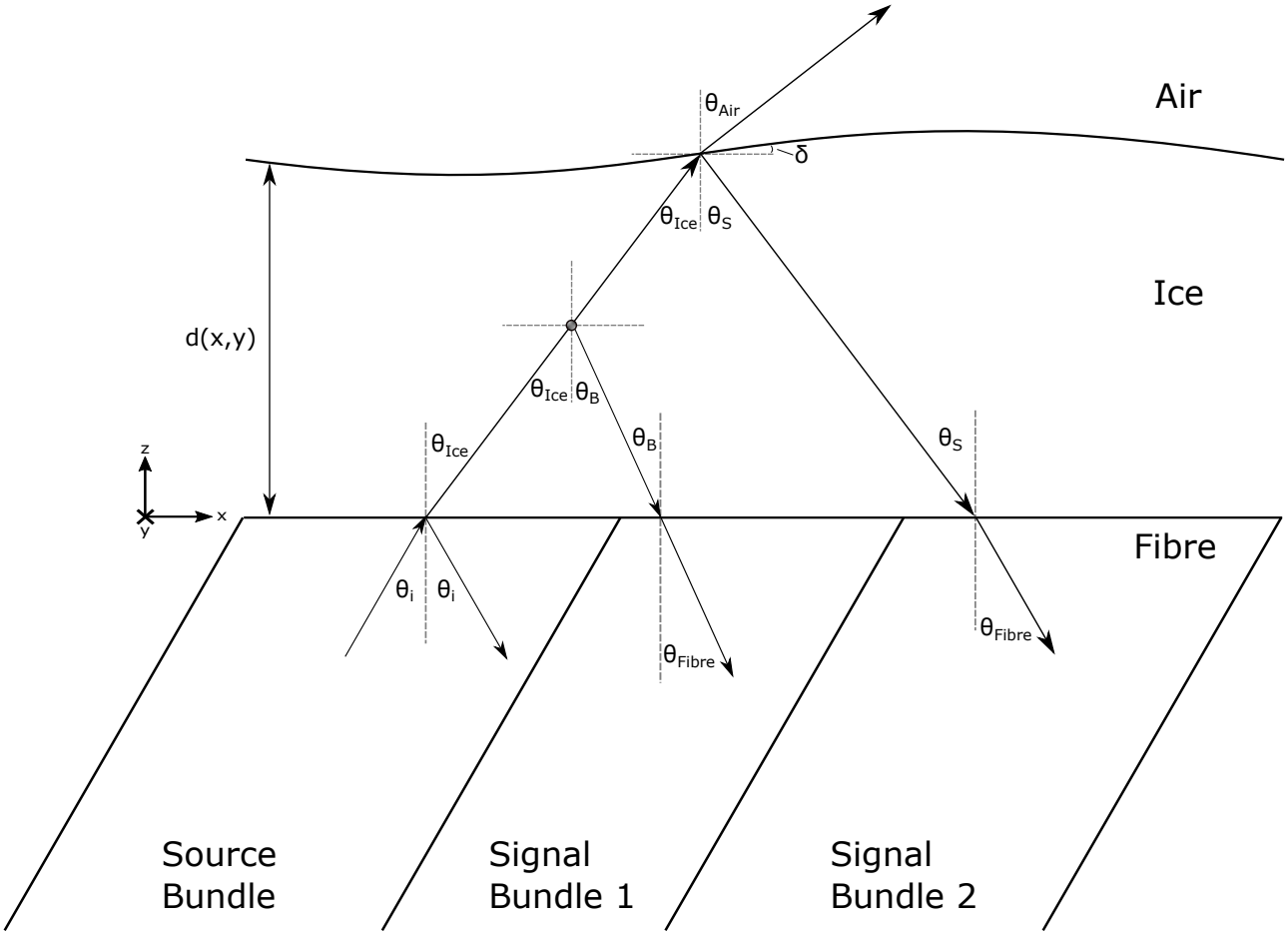

Figure 3.14: Exemplary 1D illustration of a ray propagating through the ice. After the ray is emitted by a fibre within the source bundle, it reaches a bubble and is scattered. After the scattering event, the ray is reflected at the uneven surface of the ice. The scattered ray couples into a fibre within signal bundle 1. The reflected ray enters a fibre inside signal bundle 2.

The illustration of the propagation is presented in 1D in order to depict it as clearly as possible. The computation of all steps during the simulation is carried out in 3D. d denotes the ice thickness and depends on the x and y coordinates. The corresponding angles are described in the following sections.

Fibre/Ice Interface

First of all, the transmission of a ray from a source fibre into the ice volume has to be considered. In this respect, the incident angle θ_i at this interface has to be described properly. In order to derive θ_i, some intermediary variables are required.

In Section 3.1.7 it is discussed that only rays within a certain angle θ_max are capable to perform a Total Internal Reflection inside the fibre. The rays are emitted from a light source in air. Using Equation (3.16), the angle is given by

$$\theta_\mathrm{max} = \arcsin\left(\frac{\mathrm{NA}}{n_\mathrm{Air}}\right). \tag{3.17}$$

Rays within the obtained angle θ_max from Equation (3.17) are capable of performing a Total Internal Reflection inside the fibres and are transmitted towards the fibre/ice interface.

The corresponding maximum transmitted angle inside the fibre is computed by

$$\theta_\mathrm{max,f} = \arcsin\left(\frac{n_\mathrm{Air}}{n_\mathrm{Fibre}}\sin\left(\theta_\mathrm{max}\right)\right). \tag{3.18}$$

For each fibre the angle θ_f is selected randomly. The fibre angle has values between $-\theta_\mathrm{max,f} < \theta_\mathrm{f} < \theta_\mathrm{max,f}$. This is modelled by a normal distribution with $\mathcal{N}(\mu = 0, \sigma = \frac{\theta_\mathrm{max}}{5})$. Values outside the defined range are clipped.

Without inclination, the resulting angle of a ray in ice would be

$$\theta_0 = \theta_\mathrm{Ice} = \arcsin\left(\frac{n_\mathrm{Fibre}}{n_\mathrm{Ice}}\sin\left(\theta_\mathrm{f}\right)\right). \tag{3.19}$$

As mentioned above, the computational steps are performed in 3D space. Figure 3.15 illustrates a possible direction of a ray in space as it is emitted by a fibre, which has no inclination. It can be seen that the direction of the ray is described by the angles θ_0 and β_0, where β_0 is a random angle between $0° < \beta_0 < 360°$.

By means of θ_0, β_0, the ice thickness d and the transformation of polar coordinates to cartesian coordinates, the x and y components of the ray and the corresponding angles inside the fibre $\theta_\mathrm{f,x}$ and $\theta_\mathrm{f,y}$ can be obtained.

Due to a certain inclination angle θ_Incl, the resulting incident angle $\theta_\mathrm{i} \neq \theta_f$. The inclination affects the angle $\theta_\mathrm{f,x}$ of the x component. The angle $\theta_\mathrm{f,y}$ of the y component is not influenced.

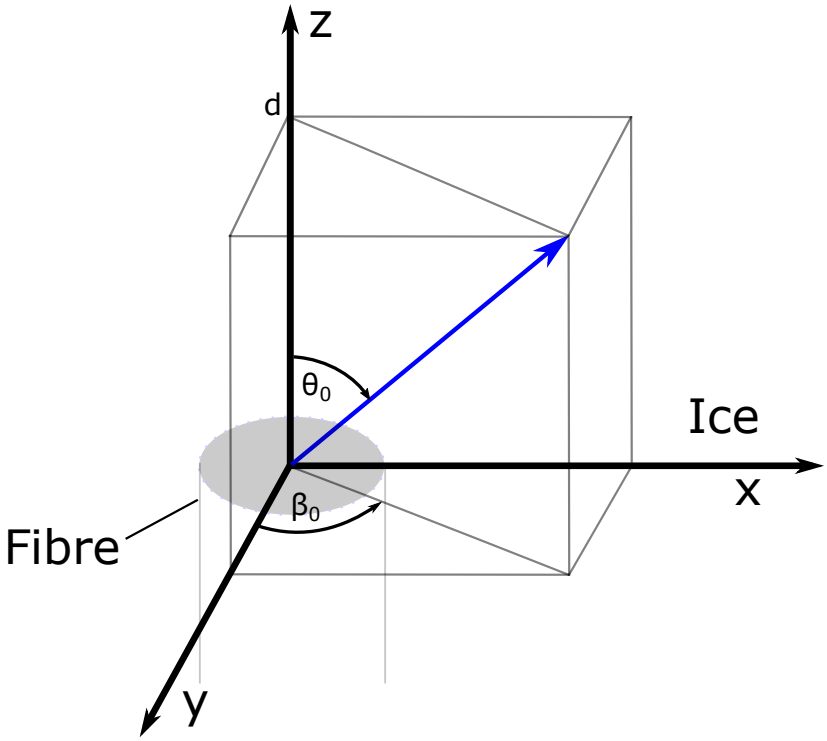

Figure 3.15: 3D illustration of ray propagating into the ice. The direction of the ray in space is described by the angles θ_0 and β_0. The fibre does not have an inclination. Hence, $\theta_0 = \theta_{\text{Ice}}$.

The influence of the inclination is described by

$$\theta_{\text{i,x}} = \theta_{\text{f,x}} + \theta_{\text{Incl}}, \tag{3.20}$$

where $\theta_{\text{f,x}}$ is the corresponding angle of the x component of the ray inside the fibre and $\theta_{\text{i,x}}$ is the deviated angle inside the fibre, which contributes to the overall incident angle θ_{i}. It can be obtained by means of the transformation from cartesian coordinates to polar coordinates.

Figure 3.16 illustrates the effect of Equation (3.20). When the surface has an inclination, the resulting angle of the x component of the incident angle $\theta_{\text{i,x}}$ is the sum of $\theta_{\text{f,x}}$ and θ_{Incl}.

The generation of the incident angles θ_{i} for each individual ray is done once during the setup of the model and not changed for the simulations at a later stage.

According to the Law of Refraction the angle of the refracted ray in ice is calculated by

$$\theta_{\mathrm{Ice}} = \arcsin\left(\frac{n_{\mathrm{Fibre}}}{n_{\mathrm{Ice}}}\sin\left(\theta_{\mathrm{i}}\right)\right). \tag{3.21}$$

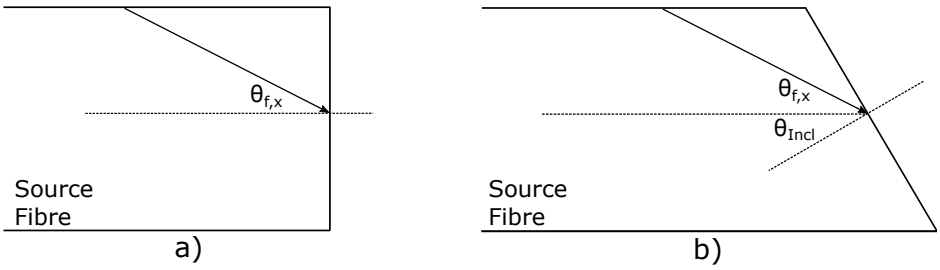

Figure 3.16: a) shows a source fibre with perpendicular surface. The angle of the x component is not affected. In b) the surface has an inclination. It can be seen that the resulting angle of the x component of the incident angle is given by $\theta_{\mathrm{i,x}} = \theta_{\mathrm{f,x}} + \theta_{\mathrm{Incl}}$.

The computation of the reflectance and the transmittance at this interface is performed by using Fresnel Equations. The result is depicted in Figure 3.17.

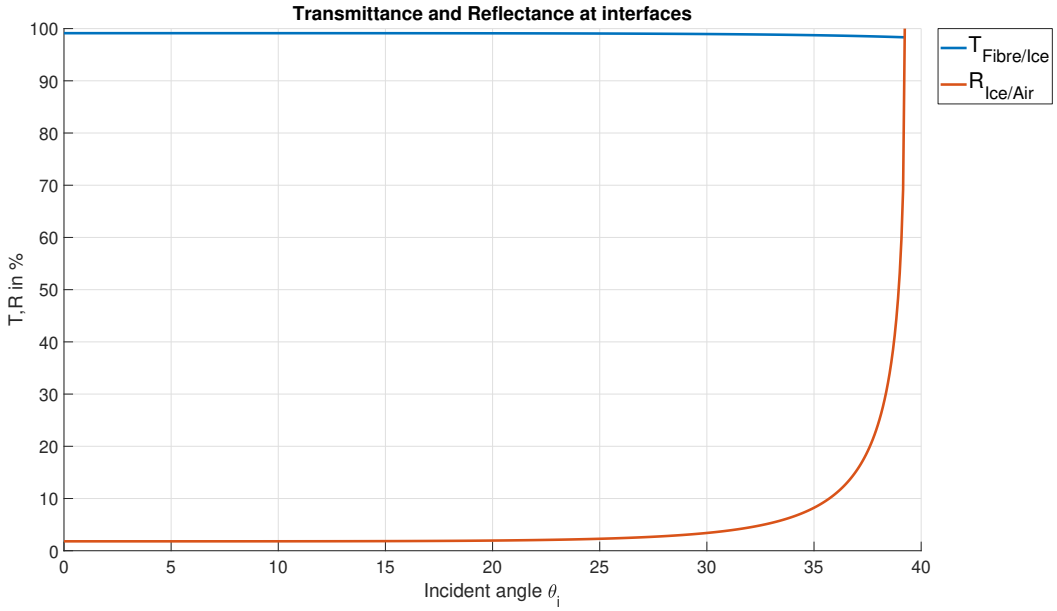

Figure 3.17: Transmittance and reflectance at fibre/ice interface as a function of the incident angle θ_{i}. For increasing θ_{i}, the reflectance also increases until the Total Reflection.

The transmittance T for the fibre/ice interface is roughly 100 % for the plotted range of the incident angle θ_i, which means that most of the light is transmitted into the ice volume. Only a small part is reflected back into the source bundle.

Scattering by Bubbles and Cracks

After the ray enters the ice volume, it reaches a micro bubble where it is scattered. The scattering event is implemented as described in Figure 3.11. The ray is split up into two rays.

One ray is forwarded without any change of direction and propagates towards the ice/air interface. As indicated in Figure 3.11, most of the power is transmitted by this ray. In the simulation the power of this ray is set to 95 % of the power of the incoming ray. The second ray is deflected by a random angle θ_B towards the fibres. The remaining 5 % of the incident flux is assigned to this ray.

Ice/Air Interface

After the scattering event the ray reaches the surface of the ice. At the surface, two angles contribute to the overall deflection:

- Angle of surface deviation δ_S: Models the local surface slope of the ice.
- Angle of diffuse reflection δ_R: Models the rough ice surface.

The sum of both angles forms the angle $\delta = \delta_\mathrm{S} + \delta_\mathrm{R}$.

The resulting angle θ_S of the reflected ray is calculated by

$$\theta_S = \theta_\mathrm{Ice} + \delta. \tag{3.22}$$

The angle δ in Equation (3.22) represents a random angle, caused by the random angle δ_R.

The angle of refraction θ_Air is computed by

$$\theta_\mathrm{Air} = \arcsin\left(\frac{n_\mathrm{Ice}}{n_\mathrm{Air}} \sin\left(\theta_\mathrm{Ice}\right)\right). \tag{3.23}$$

Figure 3.17 also shows the reflectance at the ice/air interface. It can be seen that the reflectance is very small for a wide range of the incident angle. Most of the light exits the ice volume into the air. However, there is still reflected light, which can be detected on the signal bundle areas.

Ice/Fibre Interface

The reflected and scattered rays have to be coupled into the single fibres of the signal bundles. For each ray, a coupling angle θ_{Fibre} is computed by

$$\theta_{\text{Fibre}} = \arcsin\left(\frac{n_{\text{Ice}}}{n_{\text{Fibre}}}\sin\left(\theta_{\text{S}}\right)\right) \tag{3.24}$$

and

$$\theta_{\text{Fibre}} = \arcsin\left(\frac{n_{\text{Ice}}}{n_{\text{Fibre}}}\sin\left(\theta_{\text{B}}\right)\right). \tag{3.25}$$

The Fresnel Equations are used again to compute the corresponding radiant flux of each ray.

3.2.3 Discretization in z-Direction

In order to describe the propagation of the rays in the ice volume, the thickness of the ice is discretized in the z-Direction. The discretization is done by means of a step size Δ_{Ice}.

The appearance of scattering objects within a simulation step is incorporated randomly for each discretization step. Depending on the type of ice, the probability for a scattering event P_{B} is low or high. For glazed ice, P_{B} will be low. For rime ice, P_{B} will be accordingly high.

3.3 Ray-Tracer versus Conventional Approach

In this section the result of the Ray-Tracer is compared with the result of the conventional approach as described in Section 2.1. A homogeneous flat surface and perfectly glazed ice is assumed. For this type of ice, the shape of the reflection is equal to the shape of the source bundle.

The conventional approach presented in Chapter 2 is an analytical computation of the overlapping areas of the reflection and the surface of the signal bundles.

The Ray-Tracer considers different effects during the propagation to evaluate the sensor behaviour. It computes the direction and flux for each ray individually. The radiant flux of each ray contributes to the overall radiant flux, which is detected on the signal bundles. As the surface of the ice is parallel to the surface of the sensor, all the single rays undergo a specular reflection and form the yellow reflection seen in Figure 3.18 for a certain ice thickness. As the ice thickness increases, the reflection propagates from left to right and passes signal bundle 1 and later on signal bundle 2.

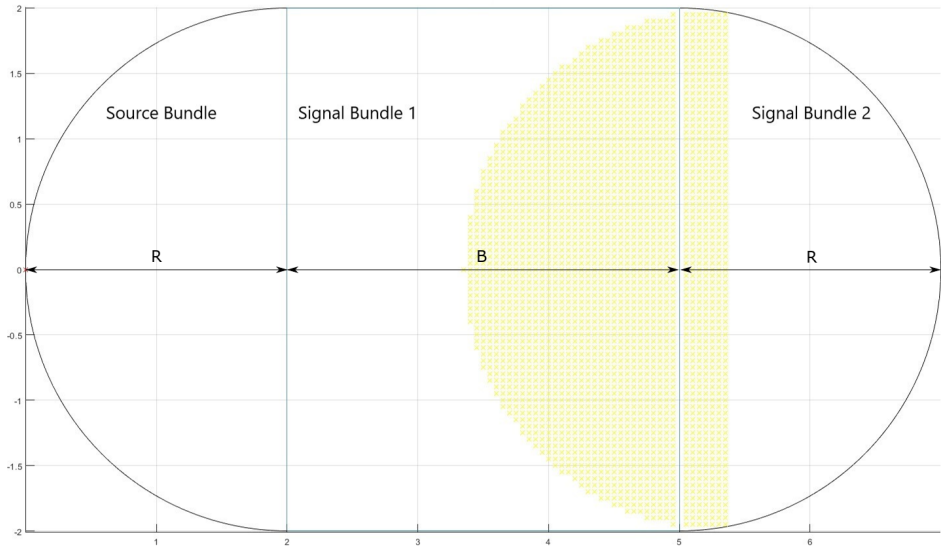

Figure 3.18: Specular reflection computed with the Ray-Tracer. Due to the ideally glazed ice and the flat surface, the reflection of the source bundle is perfectly mirrored on the sensor area.

The result of the two simulations is depicted in Figure 3.19. The blue and magenta curves depict the results of the Ray-Tracer. It can be seen that the result of the conventional approach (green and cyan) has approximately the same trend. Between an ice thickness of 1.2 mm and 1.9 mm, the reflection appears completely in the first signal bundle only. In this region the impact of the absorption is seen, as within this range of the ice thickness the radiant flux of the blue and green curves decreases slightly. Without any cracks or bubbles, the flux becomes 0 W as the reflection passes the corresponding areas.

For this simulation R = 2 mm and B = 4 mm are chosen. Further parameters are:

- Number of rays $N = 2546$
- Radiant flux for each ray $\Phi_{\text{Ray}} = \frac{5\text{mW}}{N}$
- Wavelength $\lambda = 940\,\text{nm}$
- Absorption coefficient $\alpha = 12\ \text{m}^{-1}$
- Step size for ice thickness $\Delta_{\text{Ice}} = 0.1\,\text{mm}$

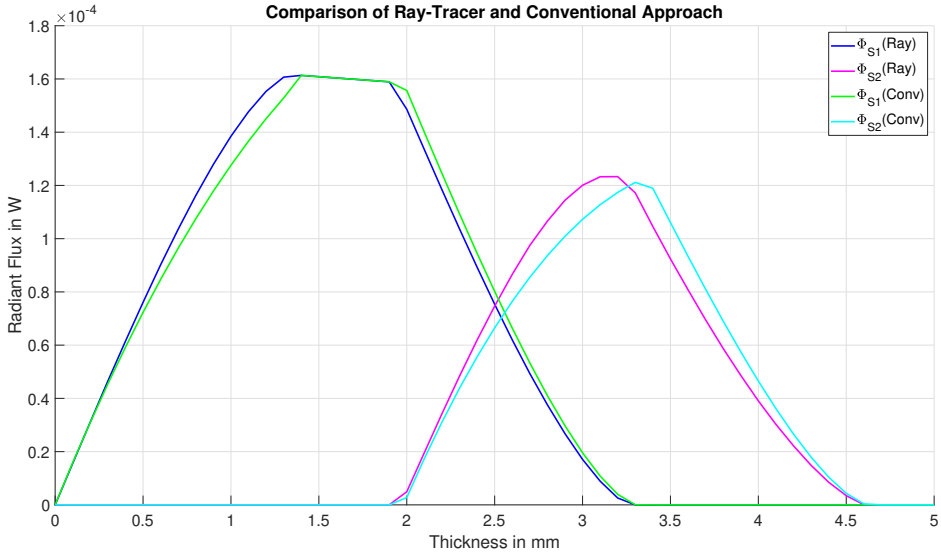

Figure 3.19: Result of the Ray-Tracer compared to conventional approach. It can be seen that the conventional approach, analytically calculating overlapping areas, can be approximated by the Ray-Tracer approach, as the resulting radiant flux are in good agreement.

3.4 Simulation of Different Ice Types

In Section 3.3 it is shown that the Ray-Tracer works for ideally glazed ice with a flat surface, as the outcome approaches the analytical solution.

It is furthermore of interest to model different types of ice as described in Section 2.1.1.

As already mentioned in Section 2.1, the incident light is split up into reflected and scattered light. The Ray-Tracer is capable of simulating this separation and evaluates the impact of the reflection and the scattered light on the sensor output.

3.4.1 Glazed Ice

This section shows the simulation result of the sensor, assuming glazed ice is accreted on the sensor area. Glazed ice contains a low amount of cracks and micro bubbles. In Figure 3.20 the resulting radiant flux as a function of the ice thickness is depicted. The signals show the same behaviour as in Figure 3.19. However, the trends are smoothed and the resulting radiant flux never reaches 0 W.

By means of the Ray-Tracer it is possible to show how the resulting flux is obtained. Figure 3.21 depicts the radiant flux of both the reflection and the scattering. The total

radiant flux for each signal bundle can be described by

$$\Phi_k = \Phi_{k(\text{Refl})} + \Phi_{k(\text{Scatter})} \ (k = 1, 2). \tag{3.26}$$

Φ_k is the total radiant flux for signal bundle k. $\Phi_{k(\text{Refl})}$ is the radiant flux generated by the reflection for the signal bundle k, and $\Phi_{k(\text{Scatter})}$ is the radiant flux created by the scattered light for signal bundle k.

It can be observed that the radiant flux of the reflection is significantly larger than the flux created by the scattering. This holds for both signal bundles. Nevertheless, there is a certain probability P_B for glazed ice that the ray is scattered by a micro bubble. As a result, a certain amount of flux due to scattering is present.

3.4.2 Rime Ice

For the simulation described in this section, rime ice is accreted on the sensor area. For this type of ice the probability for a scattering event P_B is accordingly high. As a result, a large number of cracks and bubbles is generated inside its volume. The resulting flux is depicted in Figure 3.22. Compared to the characteristic curve of glazed ice, this trend of the flux looks completely different.

The contribution of reflection and scattering is shown in Figure 3.23. The scattering dominates for this type of ice, as the light is hardly capable of reaching the ice/air interface. The total radiant flux is mainly caused by scattered light.

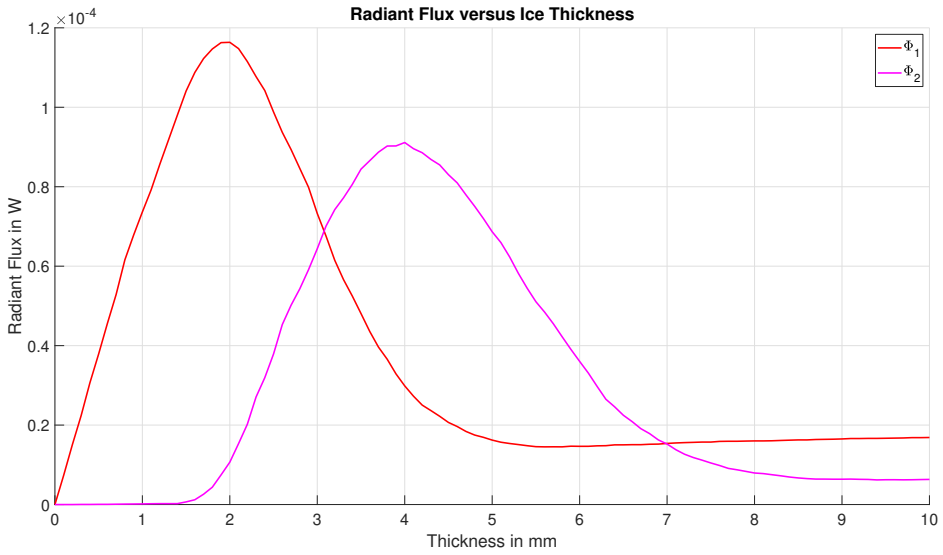

Figure 3.20: Overall radiant flux for glazed ice. Due to the low amount of air in the ice, the total flux for glazed ice is mainly caused by the reflection. With increasing ice thickness, the resulting radiant flux Φ_1 and Φ_2 increase up to a corresponding maximum. For a further increase of the ice thickness, the flux decreases again.

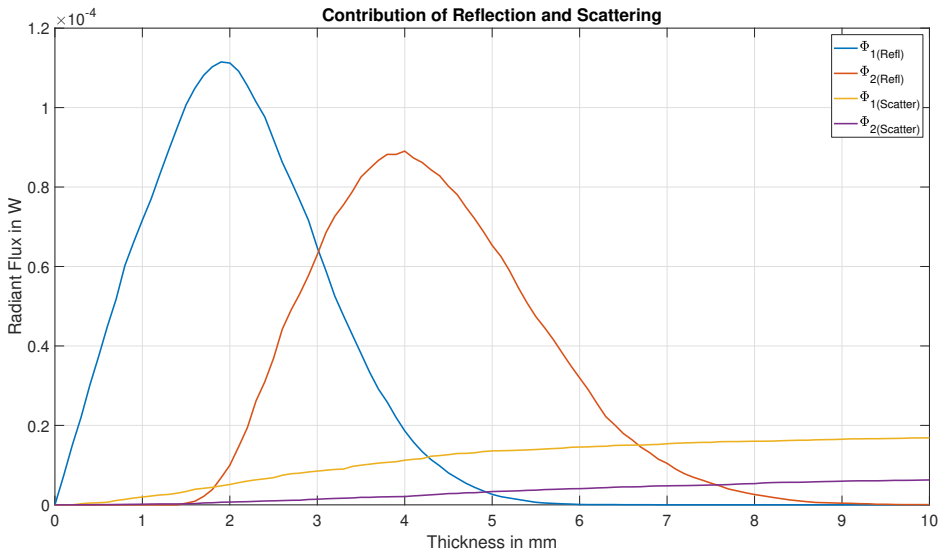

Figure 3.21: Contribution of reflection and scattering for glazed ice. Due to the low number of cracks or micro bubbles, the radiant flux from the reflection is larger than the flux from the scattered light.

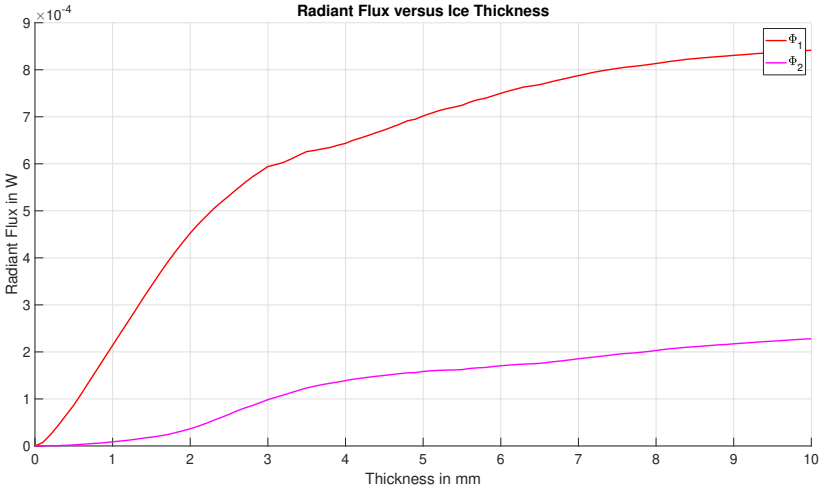

Figure 3.22: Overall radiant flux for rime ice. Due to the high amount of cracks and bubbles, the total radiant flux is mainly determined by the scattered light. As ice thickness increases, the resulting radiant flux Φ_1 and Φ_2 for each signal bundle increases as well.

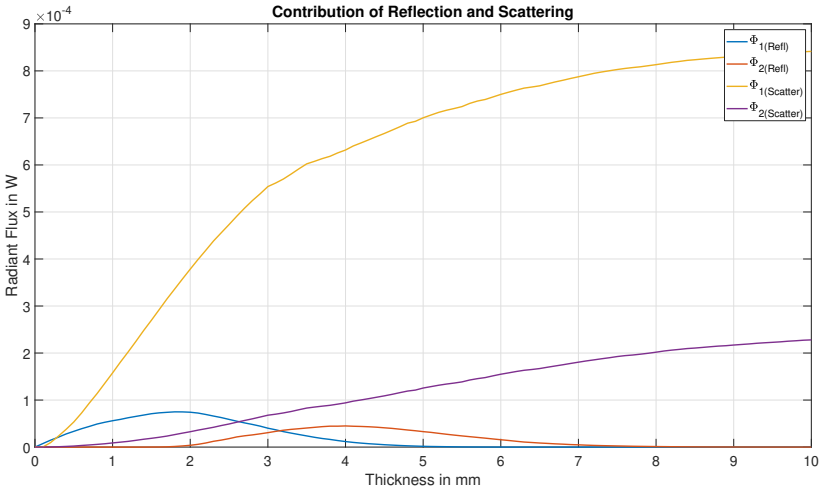

Figure 3.23: Contribution of reflection and scattering for rime ice. The radiant flux created by the scattering dominates the flux of the reflection. Due to the high amount of cracks and micro bubbles, more light is trapped inside the ice volume, leading to higher values of the flux.

4 Construction of a Sensor

This chapter presents the mechanical construction of the sensor. The sensor design is based on [16]. A closer look is given on how the sensor area is composed. The optical coupling of the light emitting and light receiving devices with the bundles is discussed in a further section.

The fibres for the sensor are taken from a flexible fibre optic light guide, which was purchased. As depicted in Figure 4.1, the coating of the light guide is cut off and the fibres are extracted.

Figure 4.1: Raw material for the construction of the sensor. The fibres are extracted from the coating and cut to a suitable length for the sensor.

The specifications of the fibres are:

- Refractive index of core (fibre) $n_\mathrm{f} = 1.581$
- Refractive index of cladding $n_\mathrm{c} = 1.487$
- Numerical Aperture NA = 0.55

Sensor Structure

The desired sensor structure is sketched in Figure 4.2 and is taken from [16]. The sensor consists of one source bundle and two signal bundles. Its surface has an inclination with an inclination angle of 30°. According to [16], this sensor is a dedicated sensor to determine the ice type. Due to the architecture with two signal bundles and a following differential evaluation by a proper electronic circuit, the ambient light can be compensated.

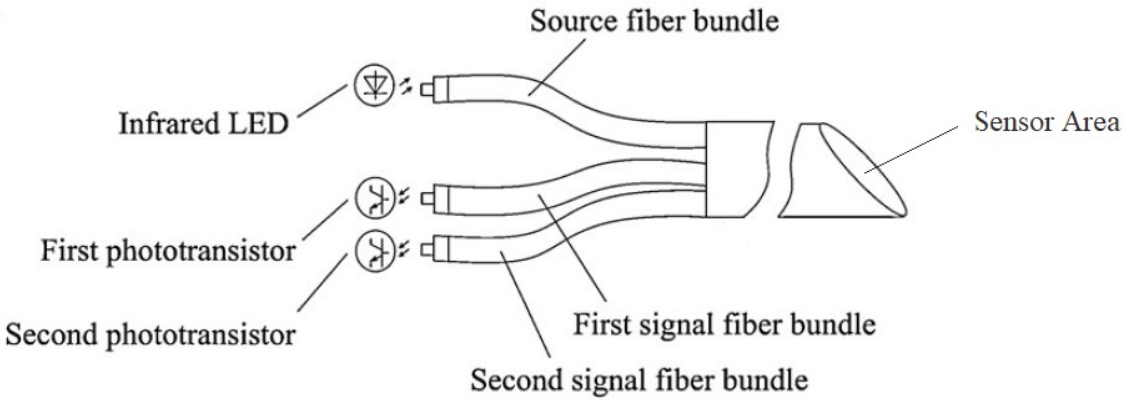

Figure 4.2: Sensor structure based on [16]. IR light is guided towards the sensor area by the source bundle. Light at the signal bundle areas is guided through the corresponding bundle and is forwarded to the phototransistors.

By means of the single fibres, the bundles are formed and merged together. The construction of the sensor is illustrated in the following sections in more detail.

4.1 Merging of the Bundles

As depicted in Figure 4.2, the actual sensor consists of one source bundle and two signal bundles. In this step it is described what the bundles look like and how they are merged in the first step.

Figure 4.3: Premerging of the fibres to form the bundles. A black electrical tape separates the bundles.

Figure 4.3 depicts the three single bundles. Each bundle is tied together with thin copper wires in order to stabilize the single fibres. The tape is used as separation between the bundles. Two sensors have been build. A sensor with an opaque tape as depicted in Figure 4.4 and a sensor with a transparent tape. The transparent tape is also suggested in [16].

The merging of the bundles is depicted in Figure 4.4. The bundles are put on top of each other. The black tape is put between the bundles.

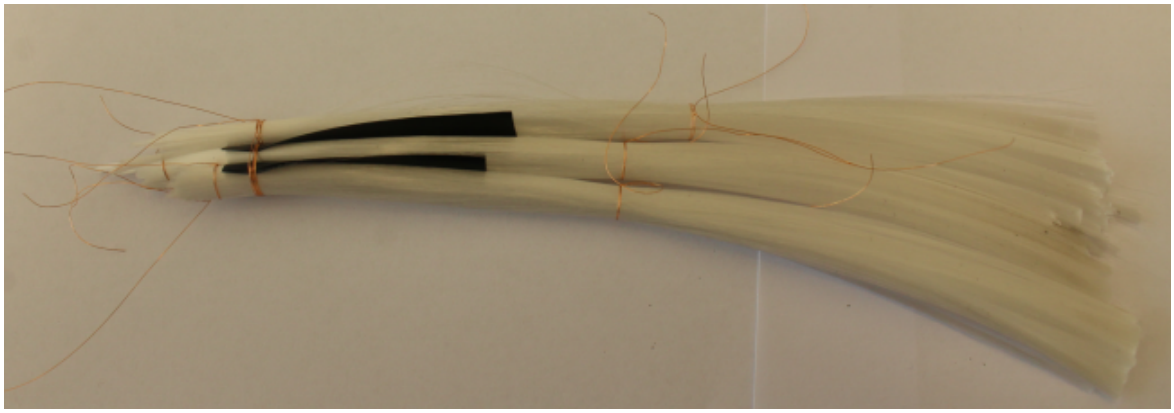

Figure 4.4: Merging of the bundles with the tape. The black tape separates the bundles and additionally gives an optical separation.

4.2 Stabilizing and Compressing of the Bundles

Once the bundles are merged, it is necessary to stabilize and compress them. It is important that the single fibres are packed together very tightly. No air should be trapped between the single fibres.

Figure 4.5: The heat shrink tube compresses the bundles. It helps to achieve the desired shape of the sensor surface.

A heat shrink tube is used for the compression. Figure 4.5 shows the compressed tube. It is essential that the black tape also sticks out of the tube to ensure an optical separation of the bundles until they are separated in a next step.

The separation of the bundles is depicted in Figure 4.6. Each bundle is individually covered with a heat shrink tube and compressed. The single bundle tubes have to sit very close to the first tube in order to avoid any influence caused by the ambient light. Small gaps can be covered up using opaque adhesive tape.

Figure 4.6: The separation and compression of the single bundles is done by means of heat shrink tubes. These are opaque and attached to the first tube as close as possible to minimize any influence of ambient light.

4.3 Mounting of the Metallic Sheath

Once the head of the sensor is compressed, it needs to be mechanically stabilized. The stabilization ensures the geometrical shape of the bundles. A metallic sheath, depicted in Figure 4.7, covers the compressed bundle. One end of the sheath provides the inclination. To hold the sheath in position, a further heat shrink tube is used.

Figure 4.7: A metallic sheath covers the main tube and the inner fibre structure. A further heat shrink tube is used to hold the sheath in its desired position.

4.4 Sealing and Polishing

The next step is the sealing of the the entire sensor with a special optical adhesive. This step is essential, as it connects the metallic sheath to the main tube. Furthermore, small gaps between the single fibres are filled with the adhesive. For the sealing, a funnel is formed and pulled over the metallic sheath. Figure 4.8 shows the sensor with

attached funnel. The fibre adhesive is poured into the funnel and then cured in an oven at around 60°C. After the adhesive is cured, the funnel is cut off.

Figure 4.8: A funnel is mounted and compressed on the sheath. The epoxy adhesive is poured into the funnel, closing tiny gaps.

The result can be seen in Figure 4.9. During the cure the transparent adhesive fills all small gaps between the single fibres. This also stabilizes the whole structure and the sheath is now sealed with the sensor head.

Figure 4.9: After the cure the funnel is removed and the transparent adhesive can be seen. The sensor head is now completely sealed, and the sheath is mounted to the main tube and the bundles.

In the next step the adhesive is cut off, as depicted in Figure 4.10. The sensor area, which is still rough and not clean at all, is already visible.

The final step involves the polishing of the sensor surface to ensure a smooth and clean surface. It is important to achieve a very clean and flat surface for every single fibre to allow the best possible light transmission into the ice volume and from the ice volume. The final sensor is shown in Figure 4.11. Due to the premerging and stabilization, the separation of the bundles can clearly be seen. The black tape is slightly bent on one side of the surface. Regardless of this, the geometric structure is suitable, and the sensor can be used for measurement experiments.

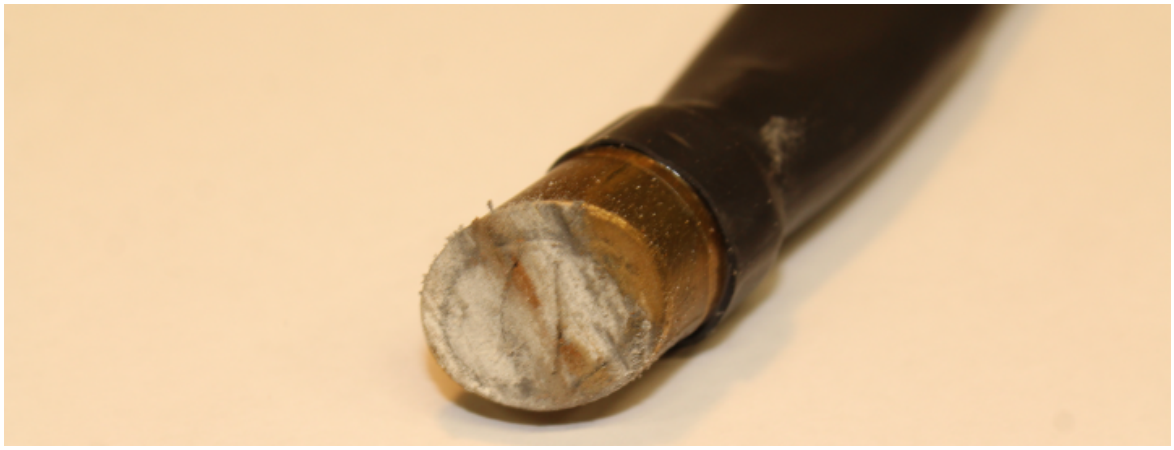

Figure 4.10: After cutting off the adhesive, the surface can already be seen. It is still rough and needs to be polished.

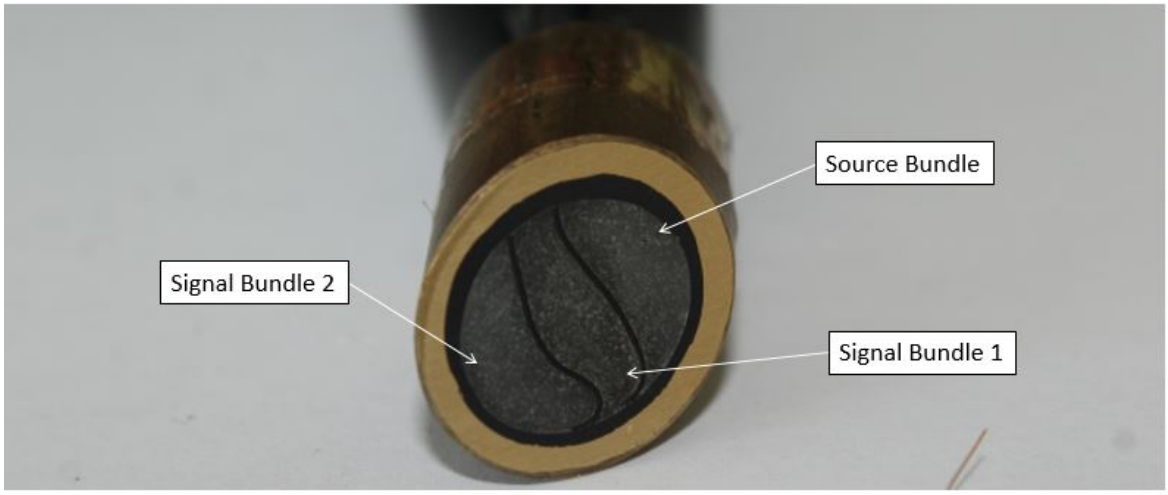

Figure 4.11: The final sensor area is completely polished. Every fibre has a smooth and clean surface to establish a suitable optical transmission.

Using the procedure as described above, two sensors are built:

- Sensor A: Transparent foil between the bundles as suggested in [16].
- Sensor B: Opaque foil between the bundles (used in all figures of this chapter).

The radius of the source bundle and signal bundle 2 is approximately 4 mm. The length of signal bundle 1 is approximately 3.2 mm.

The difference between Sensor A and Sensor B regarding the light propagation is depicted in Figure 4.12. The interface of fibre and air is taken into account.

When a ray in Sensor A reaches the fibre/air interface, it is reflected back into the source bundle. Due to the transparent foil, the reflected ray can also propagate into signal bundle 1.

With Sensor B, the opaque foil prevents the reflected light from propagating into signal bundle 1.

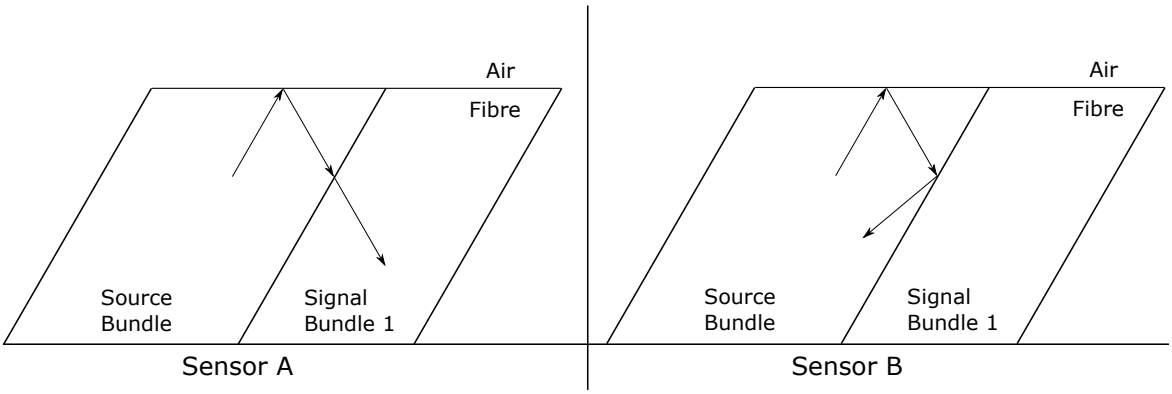

Figure 4.12: Sensor A: Transparent tape is used. The reflected ray couples into signal bundle 1. Sensor B: Opaque tape is used. No light enters signal bundle 1.

4.5 Electronic Components

Completing the mechanical construction of the sensor, the optical coupling between the bundles and the electronic components has to be set up properly. Two phototransistors are required in order to detect the light on the signal bundle areas. Furthermore, a Light Emitting Diode (LED) has to provide the necessary light for the source bundle. The selection of a LED at a wavelength of $\lambda = 940\,\text{nm}$ is based on [16], as they already showed successful results with this choice of the wavelength.

4.5.1 Phototransitor

One important function of the sensor is the measurement of the light and a proper conversion of light into an electric current. Phototransistors are devices, which are capable of transforming irradiance into an electric current. The light, guided by the signal bundles, is coupled onto the photosensitive area of the phototransistors. The photosensitive area forms the base of the transistor. Higher values of irradiance on the area lead to an increase of the Collector-Emitter current. A phototransistor is responsive in a certain spectrum. Only light within this spectrum is converted into electric current. The Spectral Responsivity of the transistor used is depicted in Figure 4.13.

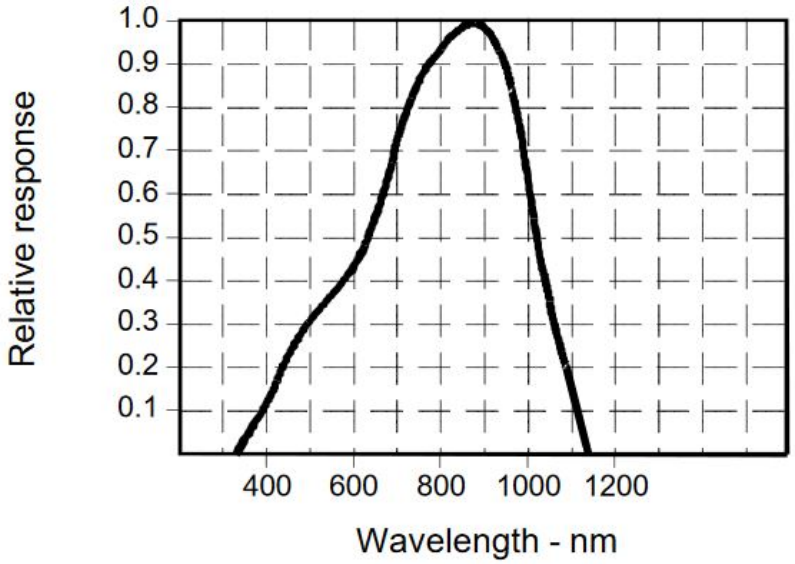

Figure 4.13: The phototransistor used is maximum responsive around $\lambda = 900\,\text{nm}$. This graph shows that not only IR light but also light at different wavelength is detected by this phototransistor [22].

Another property of a phototransistor is its acceptance angle. Inside this range of acceptance it is possible to detect light. For this particular sensor, a phototransistor

with an acceptance angle of 90° is used. The wide angle helps to detect as much light as possible in order to increase the sensitivity.

Electronic Circuit

To measure the generated currents due to the light, an electronic circuit is set up, as depicted in Figure 4.14. The photosensitive area of the transistors is illuminated by the signal bundles. The generated currents I_1 and I_2 are measured by means of two Ampere meters. The resistors R_1 and R_2 are used to generate a defined voltage drop for a possible evaluation of voltage signals as well. The currents measured are forwarded to a DAQ-system for further processing.

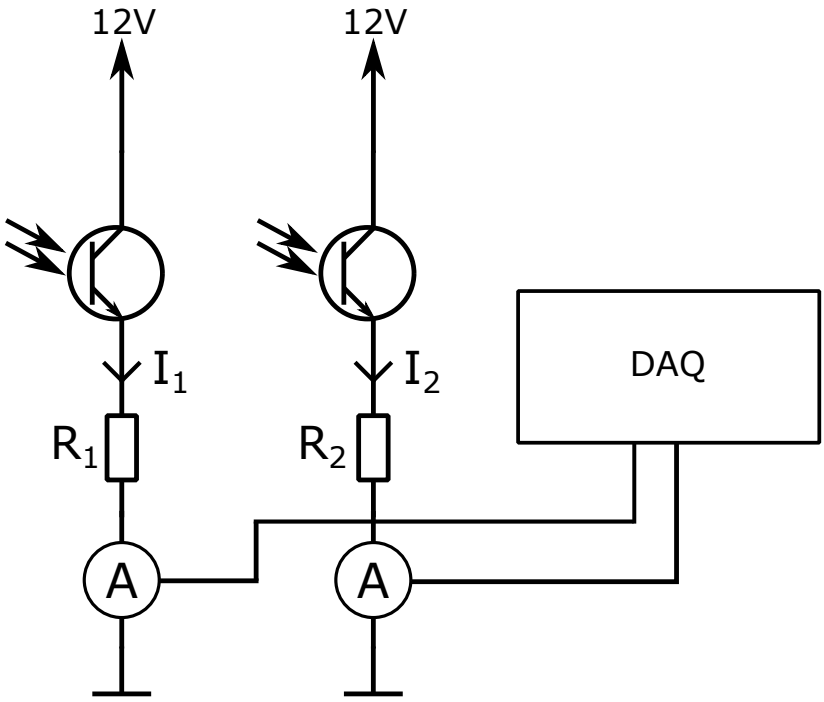

Figure 4.14: Circuit for data evaluation. The generated currents I_1 and I_2 are measured by two Ampere meters. The data is sent to a laptop to visualize and process the measured currents.

Optical Coupling of the Phototransistor

The photosensitive area of the transistor has to be illuminated appropriately in order to generate a proportional current to the incoming light. In order to collect as much light as possible, the end of each bundle is cut straight and polished. The three bundles can be seen in Figure 4.15.

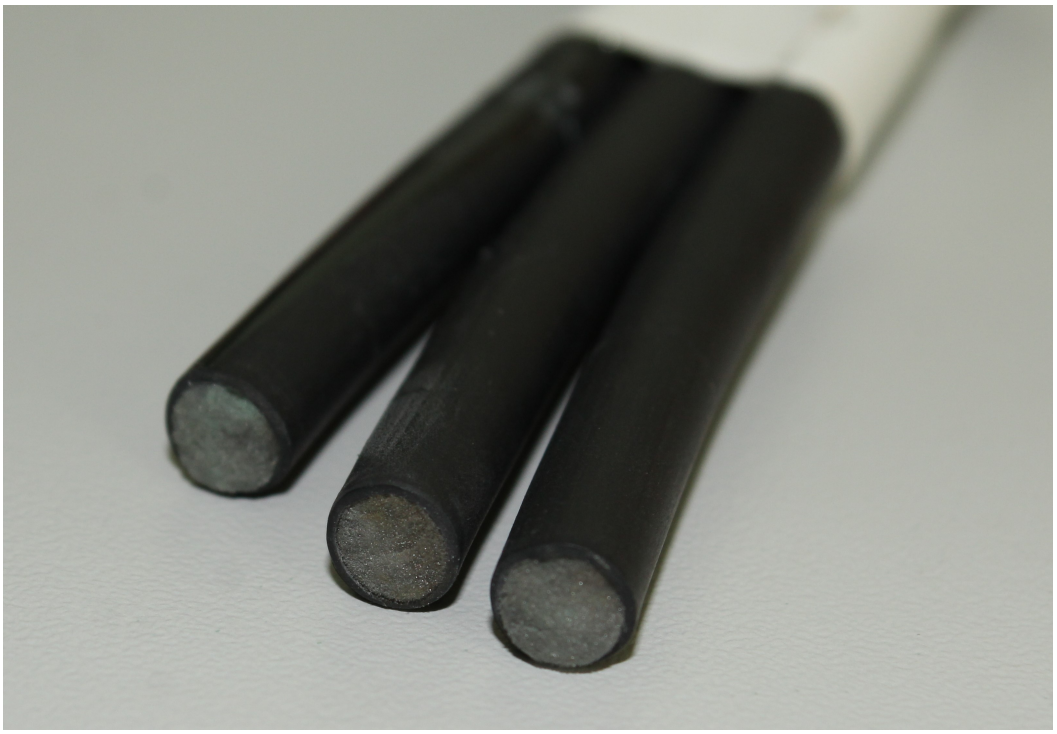

Figure 4.15: In order to establish a suitable optical connection, each of the bundles needs to have a clean and smooth surface.

The phototransistors have to be placed as close as possible to the corresponding signal bundles in order to minimize the losses between photosensitive area and signal bundle. The position of the transistor can be seen in Figure 4.16.

The last step is the shielding of the optical connection of the transistor and signal bundle. The shielding and the mechanical mounting is done by a heat shrink tube. It is opaque and also gives mechanical stability, so the device is hold in proper position. The final connection is depicted in Figure 4.17.

This step is repeated for the second phototransistor as well. Once the detectors are connected, the light emitting element has to be connected to the source bundle.

Figure 4.16: The phototransistors are placed as close as possible to the corresponding signal bundles to ensure a suitable optical transmission.

Figure 4.17: The phototransistor is connected to the bundle by means of a heat shrink tube. Due to the opaque tube, ambient light does not have any impact on the connection.

4.5.2 Light Emitting Diode

In order to provide the necessary light for the sensor, a LED is used. For this sensor a LED at wavelength of $\lambda = 940\,\text{nm}$ and a power of $5\,\text{mW}$ is chosen. The spectrum of the LED is shown in Figure 4.18. The spectrum ranges from 840 nm to 1040 nm, with a maximum value at 940 nm. The radiant intensity emitted by the LED should match the responsivity of the phototransistor in terms of the wavelength.

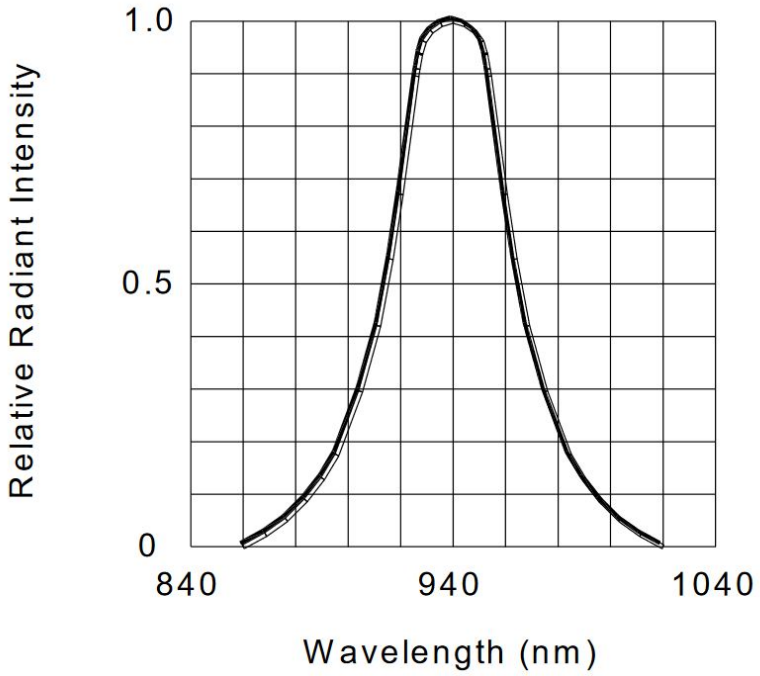

Figure 4.18: Spectrum of the radiant intensity. The spectrum shows a maximum radiant intensity at $\lambda = 940\,\text{nm}$ [23].

Optical Coupling of the LED

The optical coupling of the LED is done in the same way as for the phototransistor. The placement of the LED is depicted in Figure 4.19.

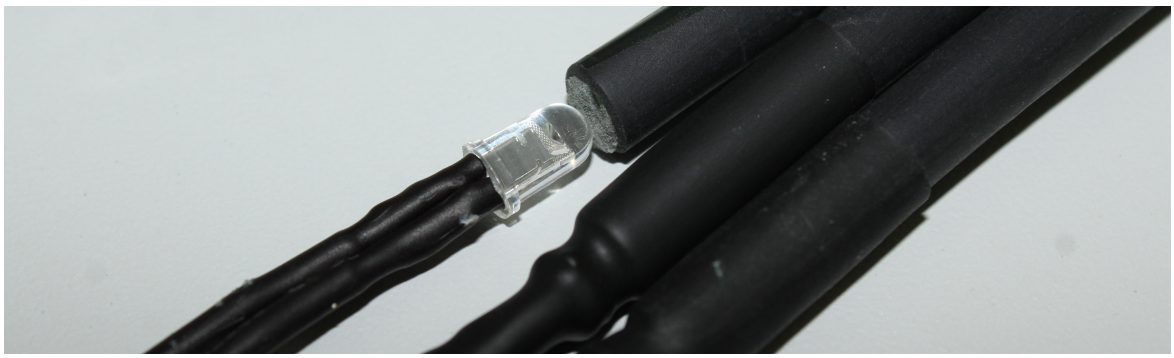

Figure 4.19: The LED is placed as close as possible to the source bundle in order to ensure that every single fibre is illuminated properly.

The completed sensor is depicted in Figure 4.20. The optical coupling of the source bundle and the signal bundles with the corresponding electronic devices is realized using heat shrink tubes. Subsequently, the area between the combined bundle and the single bundles is covered by a white opaque foil to prevent any impact from the ambient light.

Figure 4.20: Sensor with connected LED and phototransistors. The electronic components are coupled to the bundles using heat shrink tubes. An opaque adhesive is used to shield the area between the metallic sheath and the single bundles from ambient light.

An important parameter of the LED is the radiation angle. It has to be sufficient to illuminate all fibres of the bundle. This is important, as the model assumes a uniform illumination.

To make this IR area visible, a camera of a mobile phone can be used, as most mobile phone cameras do not have any IR-Filter. That means the photocells are sensitive to this region of the spectrum.

The impact of the radiation angle can be seen in both Figure 4.21 and Figure 4.22. In Figure 4.21, a LED at radiation angle of 20° is used. It can be seen that only a small part of the area is illuminated. In comparison, another LED at radiation angle of 50° is used in Figure 4.22. As can be seen, a larger part of the source bundle area is illuminated. This can be viewed even better in Figure 4.23, where the ambient light is lowered in order to allow a better look at the source bundle area. Even though the illumination is not perfectly homogeneous, the area is completely illuminated and the sensor can be used for the experiments.

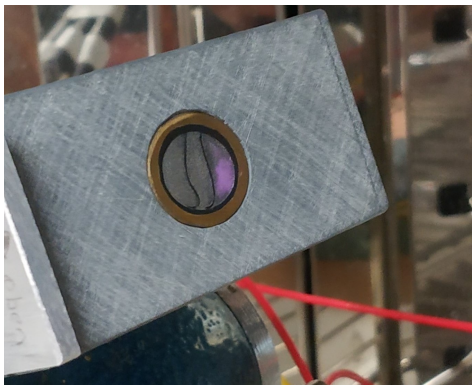

Figure 4.21: Optical coupling of a LED at radiation angle of 20°. The source bundle is partially illuminated.

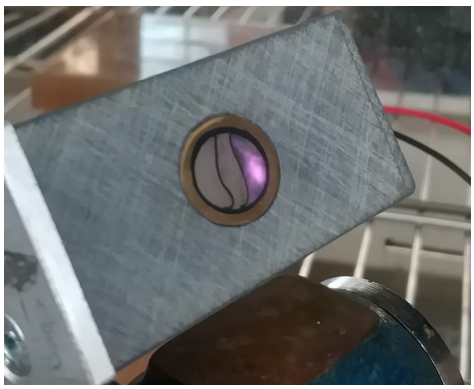

Figure 4.22: Optical coupling of a LED at radiation angle of 50°. The source bundle is completely illuminated.

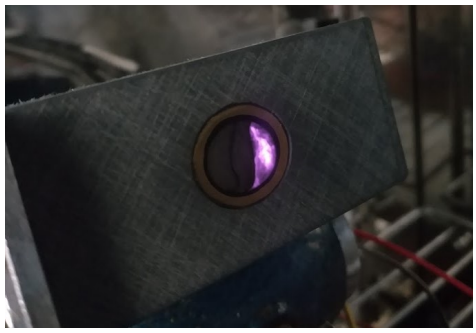

Figure 4.23: Complete illumination of the source bundle at lowered ambient light.

5 Study and Analysis of the Sensor Effect and the Sensor Behaviour

In this chapter, the constructed sensors as described in Chapter 4 are characterized and used to determine the capabilities of the FOIS for

- detecting early ice accretion and
- measuring the ice thickness for different types of ice.

In addition, the cross sensitivity with respect to water is evaluated. Furthermore, the simulation results are compared against the measured sensor signals in order to validate and calibrate the model.

The model is then used for an uncertainty analysis for the estimation of the thickness of an ice layer.

5.1 Measurement Setup and Ice Accretion

This section describes the measurement setup, which is used for the experiments. Furthermore, it is explained how different types of ice can be realized in a climatic chamber. The results of the ice accretion experiments are presented as well.

5.1.1 Measurement Setup

The overall test stand is depicted in Figure 5.1. A sprayer is connected to a nozzle outside of the climatic chamber. The supplied water is provided to the sprayer and periodically inserted into the climatic chamber. Furthermore, compressed air can be applied within the nozzle.

It is possible to generate ambient temperatures down to -40°C inside the chamber. By means of a camera in front of the climatic chamber window, high-quality pictures of inside the chamber are taken.

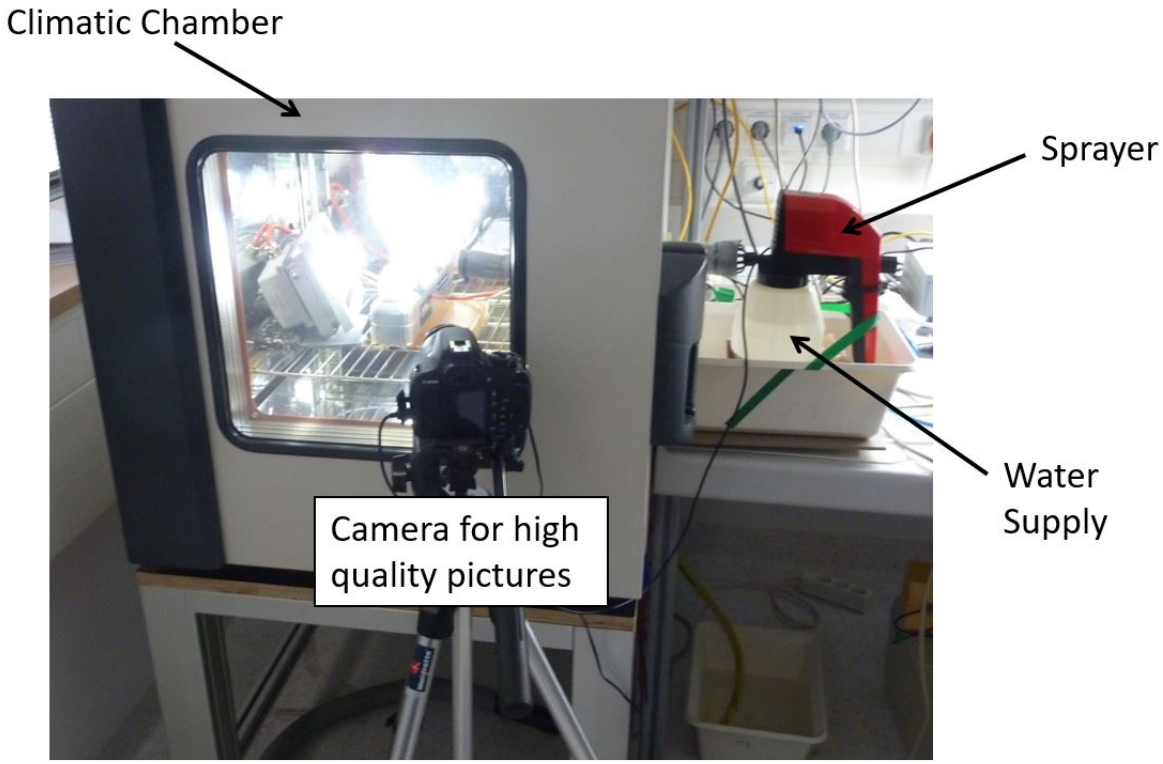

Figure 5.1: Overall test stand. The supplied water is inserted into the climatic chamber by means of the sprayer. A camera in front of chamber provides high-quality pictures of inside the chamber.

The measurement setup inside the chamber is depicted in Figure 5.2. The sensor is mounted inside a small PVC block. A bench vice is used to clamp the PVC block so that the sensor area can be tilted.

The sensor area faces the nozzle. A laser distance sensor is used as reference for the ice thickness. By means of a software the timing for the water supply, the gas injection and the camera system is controlled. A mixture of water and air is then sprayed onto the sensor surface.

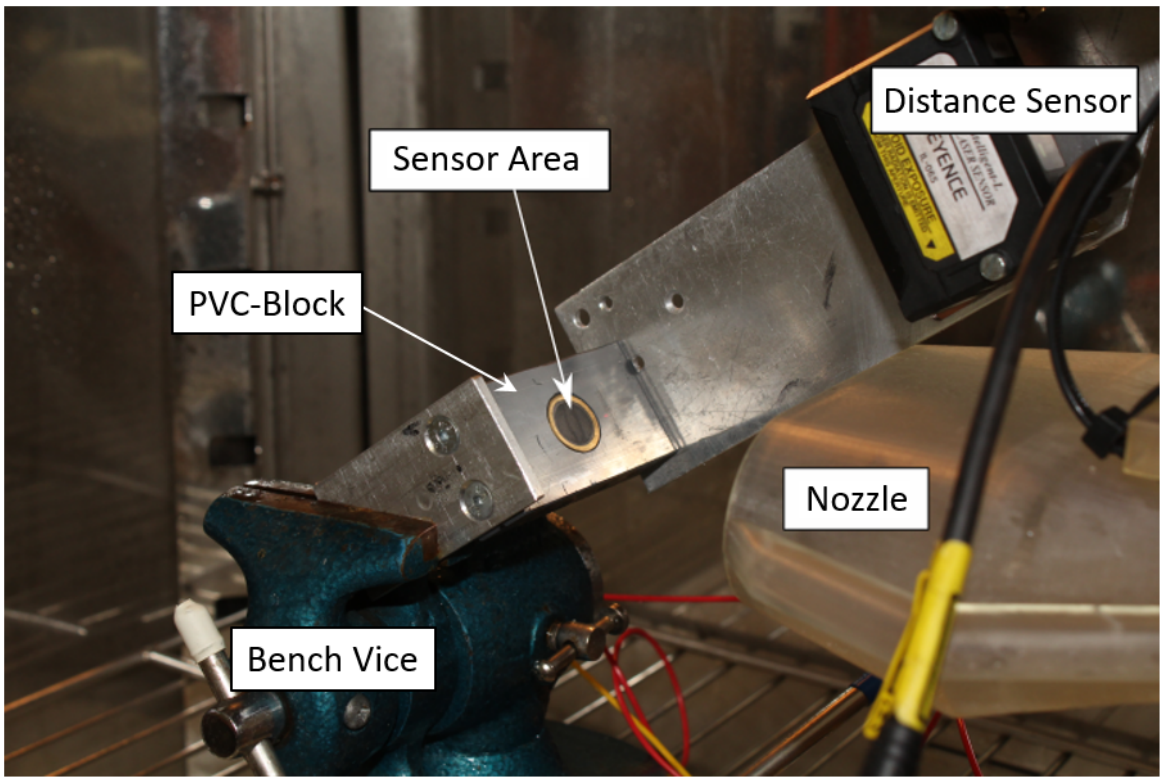

Figure 5.2: Measurement setup for ice accretion experiments in the climatic chamber. A bench vice in combination with a PVC-block forms the mounting for the sensor. By means of the nozzle, a water/air mixture is sprayed onto the sensor area. The distance sensor provides the reference height for the ice thickness.

5.1.2 Ice Accretion

This section describes how different ice types can be realized by means of the setup introduced in Section 5.1.1. Glazed ice and rime ice are accreted and the realisations of each type are presented and discussed.

The parameters regarding the timing of the water supply and chamber temperature have to be set properly for each ice type. The most important parameters are:

- Chamber temperature T_{C}
- Times t_{ON} and t_{OFF} of the sprayer
- Times t_{pre} and t_{post} for the air supply before and after the water supply

Glazed Ice

Glazed ice is characterized by its transparent ice volume. In order to realise this type of ice, hardly any air should be trapped during the ice accretion. The ice needs to form very slowly and should grow layer by layer.

The parameters are set as follows:

- $T_{\mathrm{C}} =$ -10°C
- $t_{\mathrm{ON}} = 1\,\mathrm{s}$ and $t_{\mathrm{OFF}} = 80\,\mathrm{s}$
- $t_{\mathrm{pre}} = 0\,\mathrm{s}$ and $t_{\mathrm{post}} = 0\,\mathrm{s}$

These parameters allow to spray water on the sensor for 1 s. After the spraying process, the ice has 80 s to grow before the next spray is triggered. There is no air released into the chamber, as the times for air supply are set to 0 s. The water temperature for the sprayer is about room temperature in order to allow the slow freezing process.

The PVC-Block is slightly tilted, so the water can run slowly over the sensor area. The ice can form layer by layer and hardly any air is trapped.

A realisation of accreted glazed ice is illustrated in Figure 5.3. Due to the slow freezing process of the ice, no air is trapped above the sensor area. The ice is highly transparent, as even the sensor area can still be seen.

With the described setup glazed ice of a thickness of up to 8 mm can be obtained. Ice thickness greater than 8 mm tends to capture more air and the desired transparency vanishes.

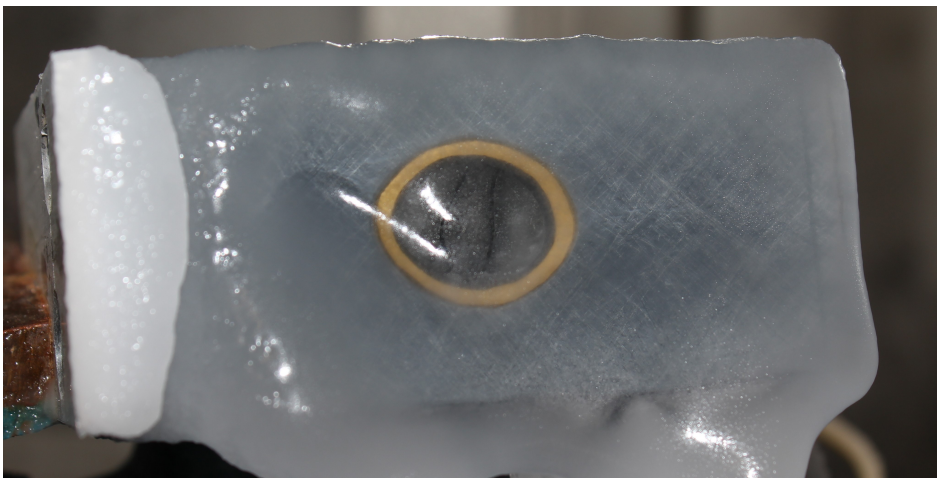

Figure 5.3: Realisation of glazed ice in the climatic chamber. Due to the slow freezing process of the water, hardly any air is trapped inside the ice volume, making the ice transparent. The sensor area can still be seen.

Rime Ice

Rime ice is characterized by its opaque ice volume, as the amount of trapped air inside the ice is relatively high. In order to realise this type of ice, the water needs to freeze rather fast. The fast freezing process ensures that a suitable amount of air is trapped within the ice.

The parameters are set as follows:

- T_{C} = -25°C
- $t_{\mathrm{ON}} = 1\,\mathrm{s}$ and $t_{\mathrm{OFF}} = 60\,\mathrm{s}$
- $t_{\mathrm{pre}} = 0\,\mathrm{s}$ and $t_{\mathrm{post}} = 1\,\mathrm{s}$

By setting these parameters, water is sprayed onto the sensor area for 1 s and then has 60 s to grow. After the spraying process, additional air is released into the chamber for 1 s to ensure a high amount of air inside the water during the freezing process.

It is important that the PVC-Block and mounted sensor are pre-cooled for about 45 minutes inside the climatic chamber. The water for the sprayer is pre-cooled as well in a fridge. The pre-cooled area of the PVC-Block in combination with the pre-cooled water and the low chamber temperature guarantee a very fast freezing process.

A realisation of rime ice in the climatic chamber is seen in Figure 5.4. The amount of air enclosed in the ice volume is very high. The sensor area cannot be seen any more.

With this setup an ice thickness of up to 15 mm is possible. This setup does not allow ice layers thicker than that, as the nozzle itself freezes, which inhibits the water supply.

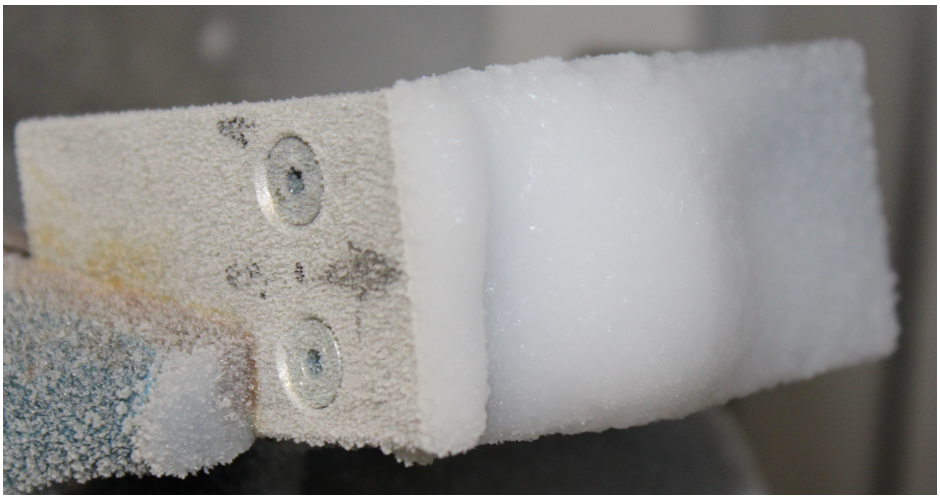

Figure 5.4: Realisation of rime ice in the climatic chamber. The high amount of air enclosed in the ice volume makes the rime ice opaque. The sensor area cannot be seen any more.

5.2 Experiments

In this section the measurement experiments are carried out in order to characterize the sensor and to evaluate its capabilities for

- detecting early ice accretion and
- measuring the ice thickness.

Measurement experiments are performed for both glazed ice and rime ice. The difference between Sensor A and Sensor B is studied.

A further experiment to evaluate the cross sensitivity with respect to water is presented.

5.2.1 Study: Glazed Ice

For glazed ice, two measurement studies are carried out to study the difference in the construction between

- Sensor A (transparent tape between the bundles) and
- Sensor B (opaque tape between the bundles).

The first series of experiments is performed with Sensor A, whereby four ice accretion experiments are carried out. In the second series, six measurements are performed, using Sensor B.

Sensor A

The results of the first series of measurements, using Sensor A, are depicted in Figure 5.5. It can be seen that the results of the experiments do not coincide with the simulation result depicted in Figure 3.20.

An offset current of $I_1 \approx 13\,\mu\text{A}$ and $I_2 \approx 2.5\,\mu\text{A}$ for an empty sensor area is seen. The arise of this offset can be explained by means of Figure 4.12, taking into account that there is not any ice on the sensor surface. Figure 3.7 shows that at an incident angle of 30° for the light, the resulting reflectance at the fibre/air interface is about 8 %. This fraction of the incident radiant flux is reflected at the fibre/air interface and propagates forward inside the first signal bundle, where it can be detected by the corresponding phototransistor.

A second effect which can be seen is the initial reduction of the current I_1 for thin ice layers of $0\,\text{mm} < d < 2\,\text{mm}$. This behaviour can be explained by the higher refractive

index of ice compared to air ($n_{\mathrm{Ice}} = 1.31 > n_{\mathrm{Air}} \approx 1$). Once ice is accreted on the sensor area, less radiant flux is reflected back into signal bundle 1, leading to a decrease of the current I_1 for ice with a thickness below 2 mm. For $d > 2\,\mathrm{mm}$, an increase of the current I_1 is seen. The ice layer at this stage of the accretion process is then thick enough, so that the reflection of the ice/air interface takes over and causes the further trend of the currents. Due to the geometrical arrangement of the signal bundles, the increase for current I_2 starts for thicker layers of the ice.

Assessment of Sensor A to Detect Initial Ice Accretion

By analysing the results of Sensor A, as depicted in Figure 5.5, one could say that an initial decrease of current I_1 is a typical indication of a start of ice formation. The amount of reduction depends on the variations of the early ice accretion and is therefore different for every experiment. It can be concluded that a reliable detection of early ice formation is not possible with Sensor A.

Assessment of Sensor A to Measure the Ice Thickness

In the case of glazed ice, the sensor signal depends mainly on the reflection of the ice/air interface. The impact of the surface deviation can also be seen in Figure 5.5. Each ice accretion has a different surface, resulting in different sensor currents. The outcome of each run of experiments differs in terms of the maximum current and its corresponding ice thickness. It can be concluded that the variation leads to a high uncertainty for the determination of the ice thickness.

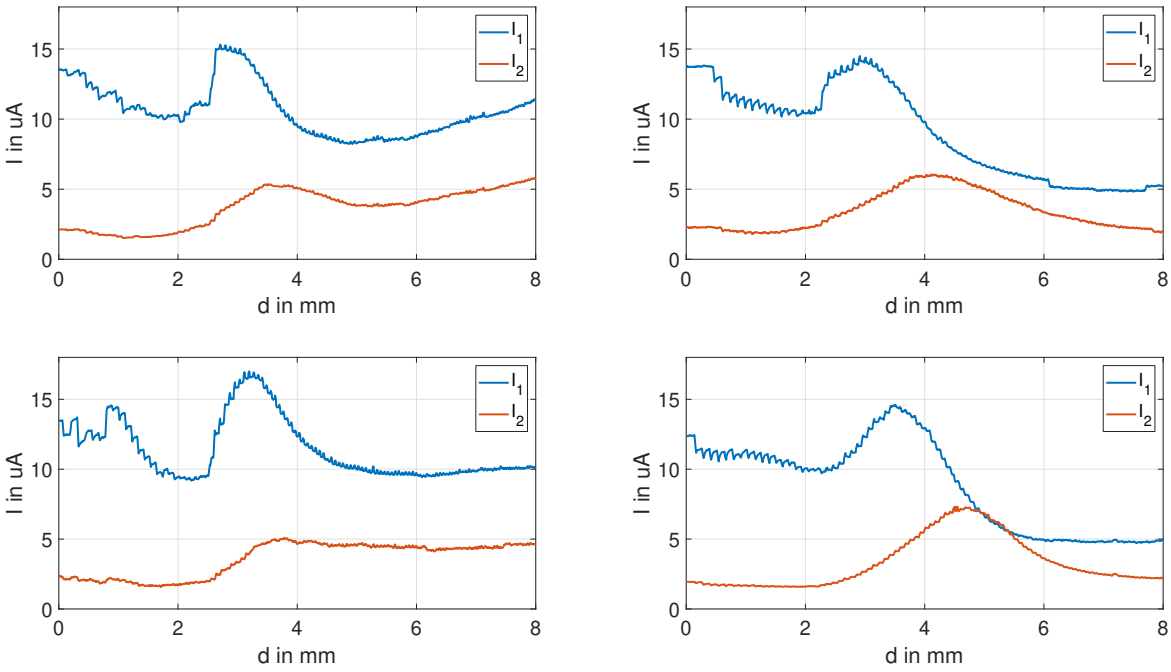

Figure 5.5: Results of the measurement experiments for glazed ice using Sensor A. Due to the transparent foil, an offset for the currents I_1 and I_2 can be seen, although no ice is accreted.

Sensor B

The results of the second round of measurement experiments, using Sensor B, are depicted in Figure 5.6. The simulation result, depicted in Figure 3.20, coincides with the results of the measurements.

The offset for both currents is not present any more. Figure 4.12 provides an explanation for this behaviour. Although no ice is accreted on the sensor area and a certain fraction of the incident radiant flux is reflected back, the reflected light is not capable of propagating into signal bundle 1. Due to the optical separation by means of the opaque tape, no light can reach the phototransistors and therefore no current is generated.

The currents start to increase for a thickness $0\,\text{mm} < d < 2\,\text{mm}$. Once ice is formed on the sensor area, the reflection at the ice/air interface immediately causes an increase of the current I_1. Another advantage of the opaque foil is the prevention of a potential cross-talk between signal bundle 1 and signal bundle 2.

Assessment of Sensor B to Detect Initial Ice Accretion

Sensor B shows a more intuitive behaviour regarding the capability of detecting ice accretion. No ice is indicated with no current. As soon as ice forms on the sensor area, the current I_1 increases immediately. This suggests that an early detection of ice accretion is possible.

Assessment of Sensor B to Measure the Ice Thickness

A reliable thickness measurement of glazed ice appears to be limited with this sensor. The impact of the random surface deviation is still present for Sensor B, as the currents vary significantly for each ice accretion process.

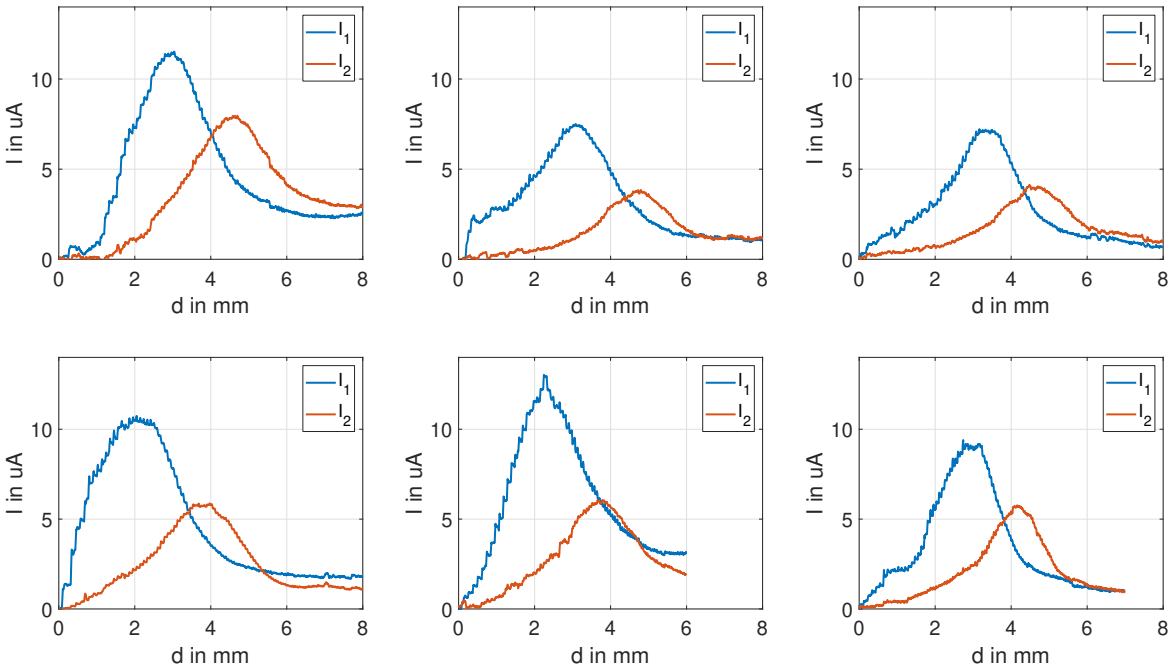

Figure 5.6: Results of the measurement experiments for glazed ice, using Sensor B. The currents I_1 and I_2 do not show an offset in the case of no ice due to the optical separation of the bundles.

5.2.2 Study: Rime Ice

For this series of experiments, involving six accretion processes of rime ice, only Sensor B is used, as it is more practical in detecting early ice accretion. The results of these measurement experiments are depicted in Figure 5.7. The simulation results, depicted in Figure 3.22, coincide well with the results of the experiments.

A first difference compared to glazed ice are the current levels. Especially current I_1 rises up to values greater than 25 µA for ice layers smaller than 2 mm. This is twice as high as the current levels for glazed ice at this thickness value of the ice. This means that more light reaches the corresponding signal bundle area.

This behaviour can be explained by looking at Figure 3.17. For glazed ice, the value of the reflectance at the ice/air interface for an incident angle of 30° is about 4 %, which means that 96 % of the light exits the ice volume and is lost. With rime ice, on the other hand, the situation is quite different. Due to the high amount of air trapped inside the ice, hardly any light is seen on the ice/air interface, as it is frequently scattered in the ice volume. Inside the accreted ice, more light is available that is capable of illuminating the signal bundle areas.

A further observation is that the value of current I_1 is roughly three times larger than the value of current I_2 for $d = 15\,\text{mm}$. The reason for this gap is that the incident light is scattered in all directions, leading to a local illumination spot above the source bundle area [14]. Since the area of signal bundle 1 is located closer to this spot, more light is seen on the first signal bundle area than on the second signal bundle area.

Assessment of Sensor B to Detect Initial Ice Accretion

Due to the immediate increase of current I_1 for ice layers smaller than 2 mm and its high absolute values, a reliable early ice detection for rime ice is possible with Sensor B.

Assessment of Sensor B to Measure the Ice Thickness

Although there is a deviation between the single sensor currents for each accretion process, the variations are in a manageable range. A slight drop of current I_1 is seen for $2.5\,\text{mm} < d < 5\,\text{mm}$. In this range, the reflection still has an impact. However, for $d > 5\,\text{mm}$, the current steadily increases. As the light is scattered in different directions and the impact of the surface is not significant, the repeatability of similar sensor signals for different rime ice accretions is possible. An evaluation of the ice thickness is feasible with Sensor B.

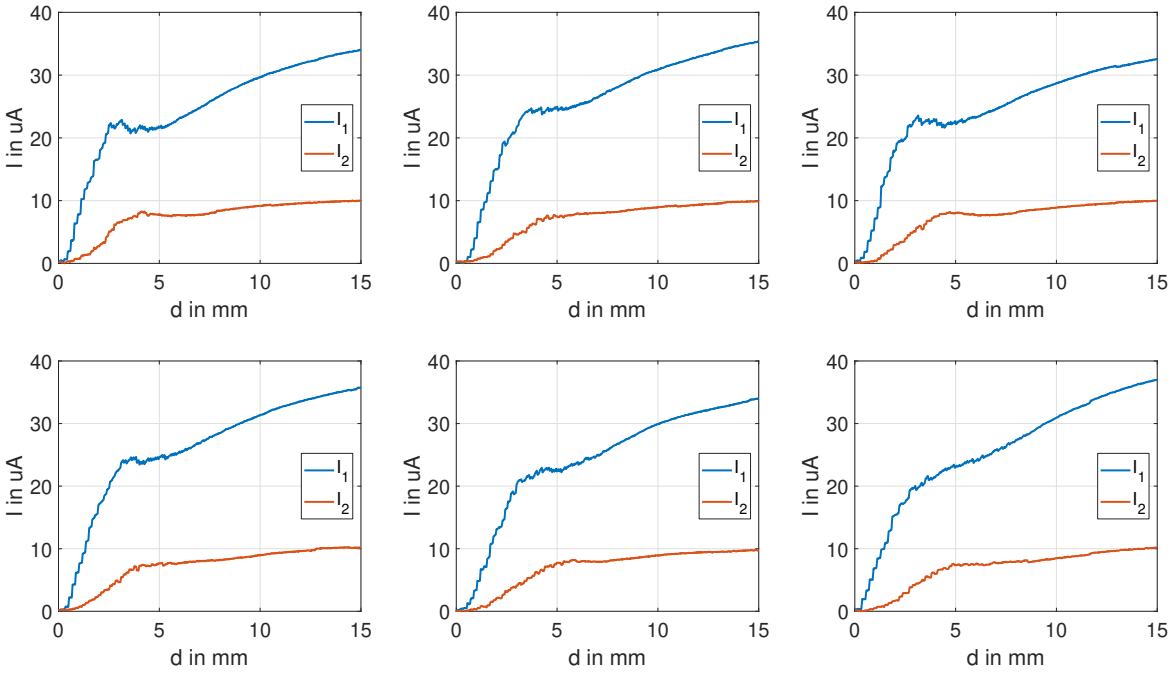

Figure 5.7: Results of the measurement experiments for rime ice, using Sensor B. It is seen that the difference between each single measurement is not significant, as the light is scattered in any direction and therefore the impact of the surface deviation is not significant.

5.2.3 Cross-Sensitivity

In order to obtain information about a possible cross-sensitivity with respect to water, a further experiment is performed. The setup is depicted in Figure 5.8. The sensor is placed in a tub, which can be filled with clear water. The water height is measured with a ruler inside the tub.

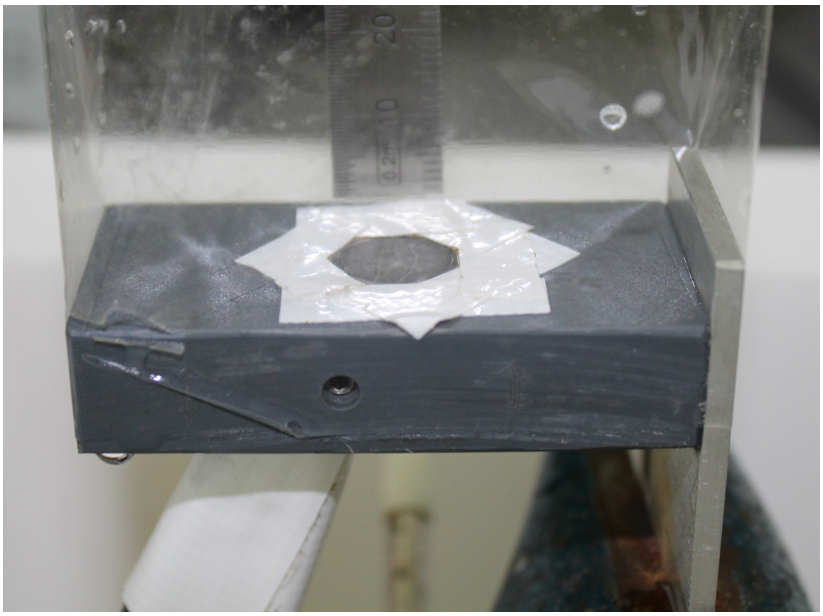

Figure 5.8: Measurement setup for evaluating the cross-sensitivity with respect to water. The tub is filled step by step with water and the corresponding currents are measured.

The results of the measurements of the currents at different stages are depicted in Figure 5.9. For clear water, the sensor behaves similar to glazed ice. Two distinct trends arise. The maxima of the currents are in the same range as the currents for glazed ice.

The reason for this result is due to the optical property of water regarding the refractive index. According to [20], the refractive index of water is $n_{\mathrm{H_2O}} = 1.33$. The refractive index of ice is $n_{\mathrm{Ice}} = 1.31$. Hence, water and ice have approximately the same refractive index. Furthermore, the water has no air included in its volume. Therefore, the characteristic trends for glazed ice and water are almost equal to each other.

The demonstrated cross-sensitivity poses a potential issue for early ice detection. In a future signal processing system, a different sensing modality, e.g. the temperature, should be considered.

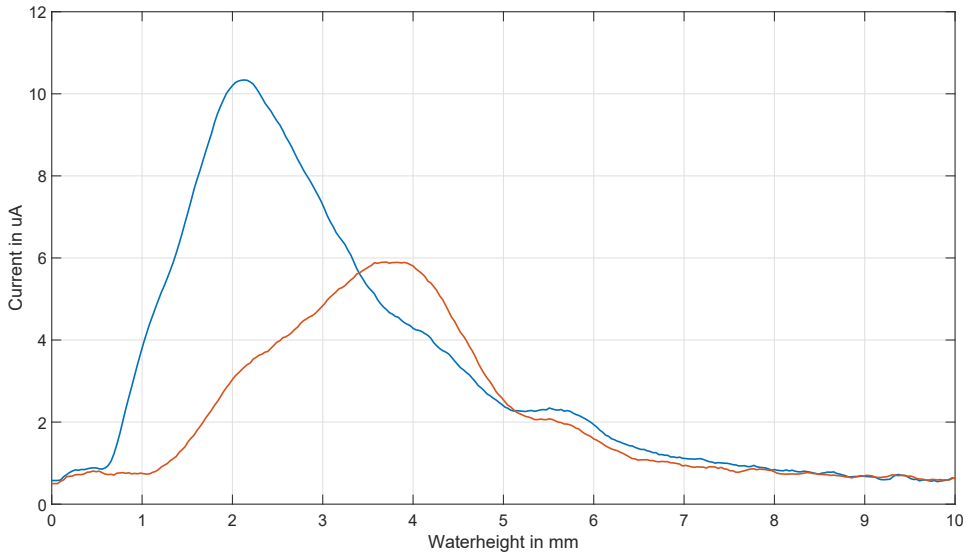

Figure 5.9: Result of the tub experiment. Two distinct trends arise for the current I_1 (blue) and the current I_2 (red). The maximum current and the corresponding water height are in the same range as for glazed ice.

5.3 Simulation and Model Calibration

In this section simulation studies using the Ray-Tracer are presented. The simulation considers the random nature of the ice accretion. It is illustrated how the surface deviation and the ice types are modelled.

5.3.1 Surface Deviation and Diffuse Reflection

Ice accretion is a random process. The surface of an ice will not be a plane parallel to the sensor surface. The modelling of this unevenness is a challenging problem.

Compared to the accreted ice area, the sensor area itself is small. The sensor can only observe a small area of the ice volume. Therefore, the deviation of the surface is modelled as a tilted plane. The plane is placed above the center of the sensor area. The plane is tilted around this central point. The slope in both x and y direction is generated by two random angles. For every accretion process a new surface is generated. The height of the ice layer depends on the x and y coordinate. Following [5], the true height is defined as the average height of the ice above the sensor. In addition, the diffuse reflection is implemented by another random angle for each new ice layer.

One exemplary realisation of such a surface is depicted in Figure 5.10. The angles for the slope of the plane in x and y direction are set at 10°. The blue dots show the projection of the source bundle onto the inclined surface. The projection is not ideal, as the random incident angle for each source fibre leads to a blurring of the projection. The yellow dots depict the diffuse reflected rays, which reach the areas of the signal bundles. The green dots represent reflected rays outside the signal bundle areas, which cannot be detected any more. The true thickness of this ice accretion is $d_{\text{true}} = 3\,\text{mm}$. The diffuse reflection is included here as well, as each ray is additionally deflected by a random angle at the surface.

5.3.2 Ice Types

The second random effect, which is included in the simulation, is the occurrence of micro bubbles. Figure 5.11 shows a simulation including randomly generated bubbles for glazed ice. The cyan circles represent the bubbles inside the ice volume. The red crosses represent the scattered rays at the bubbles. Due to the random deflection angle at the bubble, the scattered ray does not necessarily reach a signal bundle area. Depending on the ice type, a different probability is given that a ray is scattered by micro bubble and therefore the amount of bubbles is randomly generated. For glazed ice, hardly any bubbles are generated. For rime ice the number of bubbles is accordingly high.

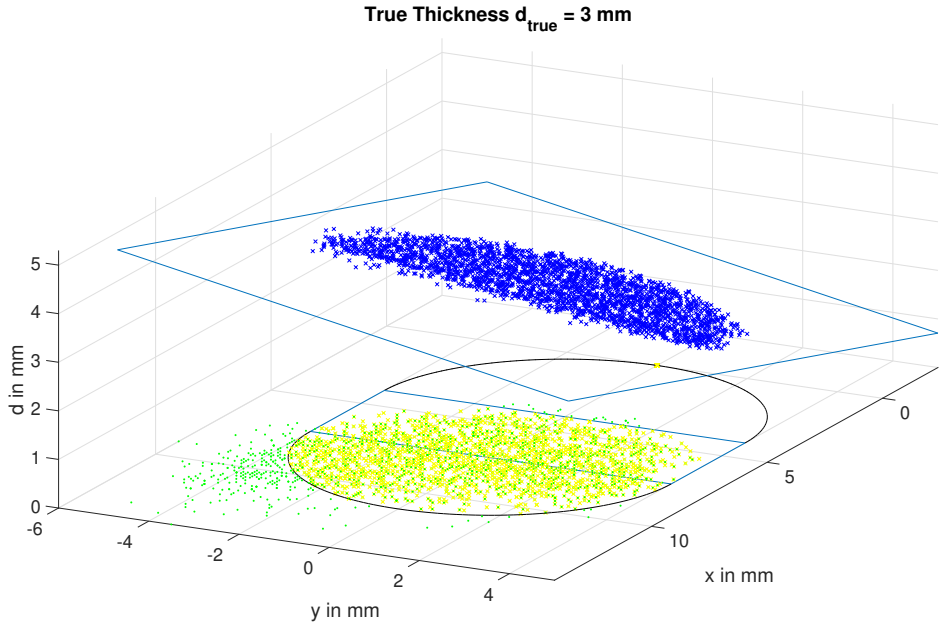

Figure 5.10: Simulation of glazed ice accretion for a true thickness of $d_{\text{true}} = 3\,\text{mm}$. The tilted plane represents the surface deviation. The blue dots represent the blurred image of the source bundle. The yellow dots are the detectable reflected rays on the sensor area. The green dots are not detectable rays. In order to present the inclined plane, the bubbles are not plotted.

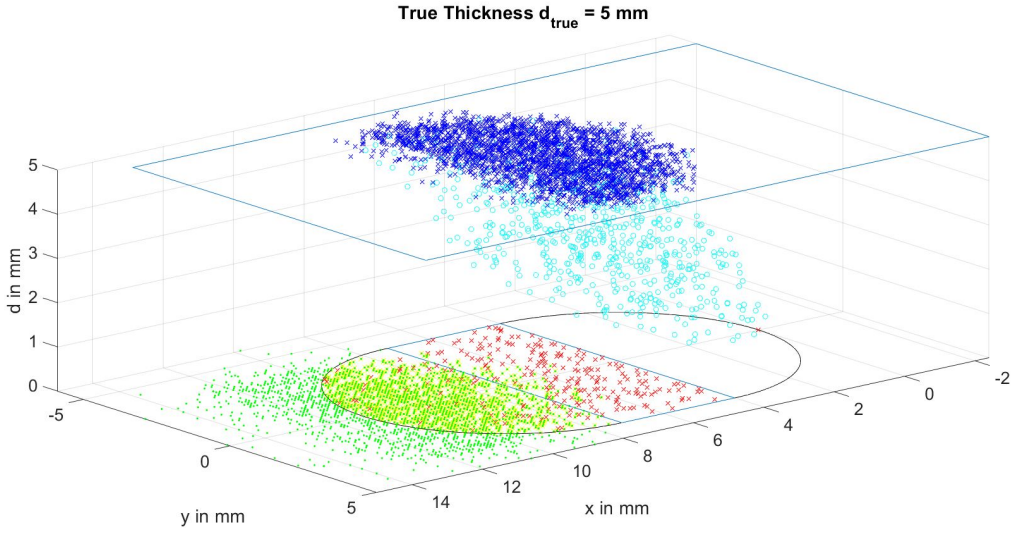

Figure 5.11: Simulation of glazed ice for a true thickness of $d_{\text{true}} = 5\,\text{mm}$. The ice volume encloses randomly generated bubbles (cyan circles). The red crosses represent the light scattered by the bubbles.

Both effects, which are shown explicitly in Figure 5.10 and Figure 5.11 are combined for the entire simulation. The following parameters are used for the simulations:

- Radius of source bundle and signal bundle 2 $R = 4\,\mathrm{mm}$
- Length of signal bundle 1 $B = 3.2\,\mathrm{mm}$
- Number of rays $N = 2546$
- Radiant flux for each ray $\Phi_{\mathrm{Ray}} = \frac{5\mathrm{mW}}{N}$
- Wavelength $\lambda = 940\,\mathrm{nm}$
- Absorption coefficient $\alpha = 12\ \mathrm{m}^{-1}$
- Step size for ice thickness $\Delta_{\mathrm{Ice}} = 0.1\,\mathrm{mm}$

These parameters are fixed for all simulations and are not changed any more. In order to model the surface slope, the diffuse reflection and the amount of bubbles, some values have to be adjusted as follows:

- Range of random angles for tilted surface δ_S
- Range of random angles for diffusive reflection δ_R
- Probability of a ray being scattered by a bubble P_B

5.3.3 Glazed Ice

In this section, the model parametrization for glazed ice is presented. In order to adjust the parameter of the simulation, the results of the measurement experiments, which are carried out for a final thickness of 8 mm, are depicted in Figure 5.12. The results can be seen in Section 5.2.1.

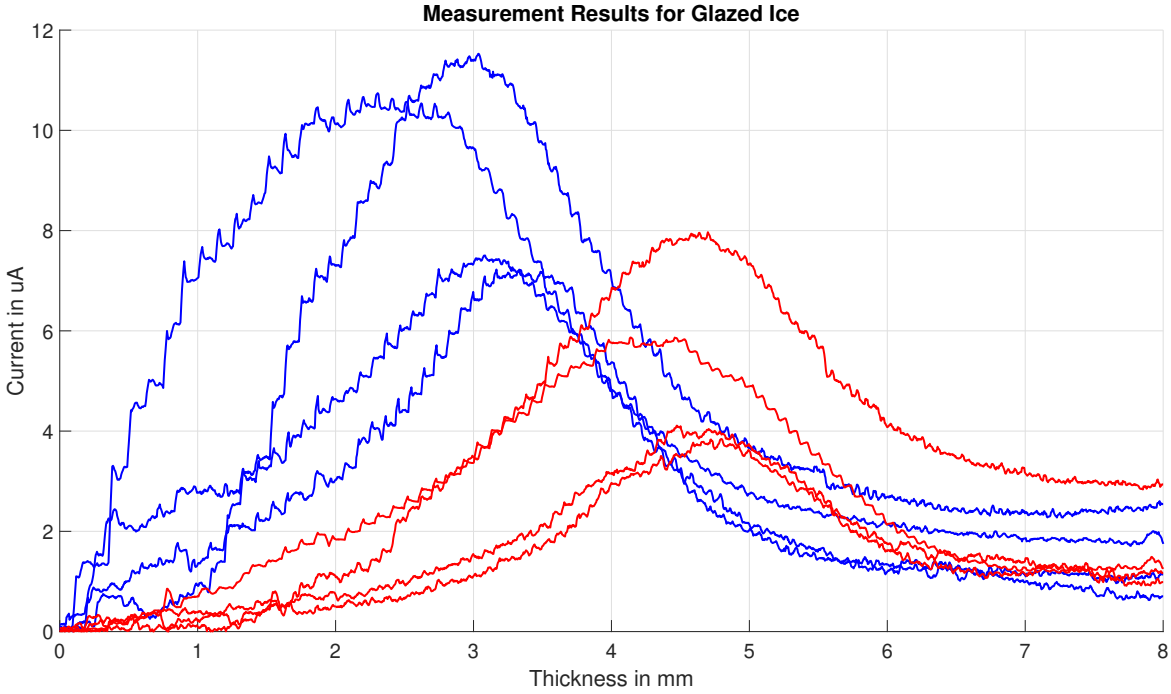

Figure 5.12: Combined plot of the measurement experiments for glazed ice. The variation of the currents I_1 (blue) and the currents I_2 (red) is due to the impact of the surface.

In the first simulation, the impact of the diffusive reflection is neglected. Hence, δ_R is set to 0°. The other parameters are set as follows:

- $\delta_S \sim \mathcal{U}$(-15°,15°)
- $P_B = 0.0015$

The simulation result for glazed ice is shown in Figure 5.13. It can be seen that a different result for the current I_1 (blue) and for current I_2 (red) is obtained for every single simulation. The trends of the measurement results and the simulation results coincide. Nevertheless, there are still differences between the results. Because in glazed ice the probability of a scattering event is low, the reflection of the ice/air interface, which depends on the tilted plane, is responsible for the different maximum currents

and its corresponding ice thickness.

The impact of the occurring bubbles can be observed because the currents for thickness greater than 5 mm do not decrease to 0 µA.

The outcome of the simulation illustrates the impact of the ice surface, as its deviation causes the variation of the sensor currents. However, the different trends of the simulation still look smooth compared to the noisy signals of the measurements. By a noise analysis of the measurement system it was found that these deviations are not due to the measurement noise. The reason for this is, that this simulation is carried out without the influence of the diffuse reflection. Despite the surface being tilted, the single rays still undergo a specular reflection.

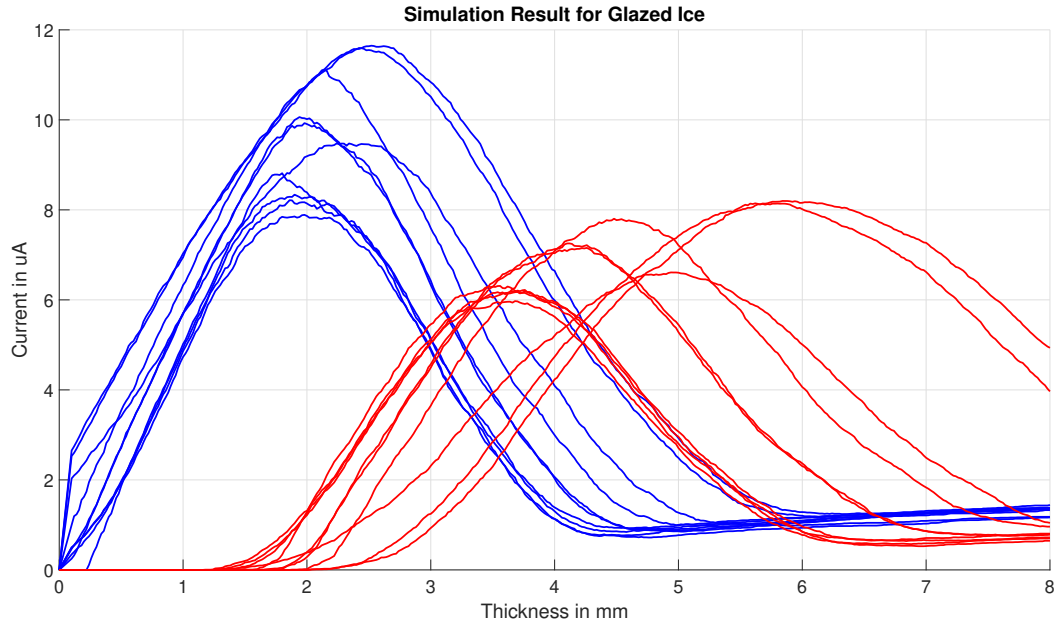

Figure 5.13: Simulation results for glazed ice including a random surface deviation. Due to the high dependency of the surface and its deviation, the currents I_1 (blue) and I_2 (red) deviate from each other for every single simulation.

The impact of the diffuse reflection is seen in Figure 5.14. For this simulation the values for δ_S and P_B are the same as in the previous simulation. The additional angle $\delta_R \sim \mathcal{U}(\text{-}30°,30°)$ is a further random parameter and represents the diffuse reflection at the surface in every new ice layer.

The diffuse reflection varies the amount of rays detectable on the signal bundles and makes the signal currents appear noisy.

Furthermore, it can be seen that also the resulting absolute currents for each ice accretion process are lower compared to the signal levels in Figure 5.13. The diffuse reflection generally lowers the amount of detectable rays and therefore the signal level of the currents decreases.

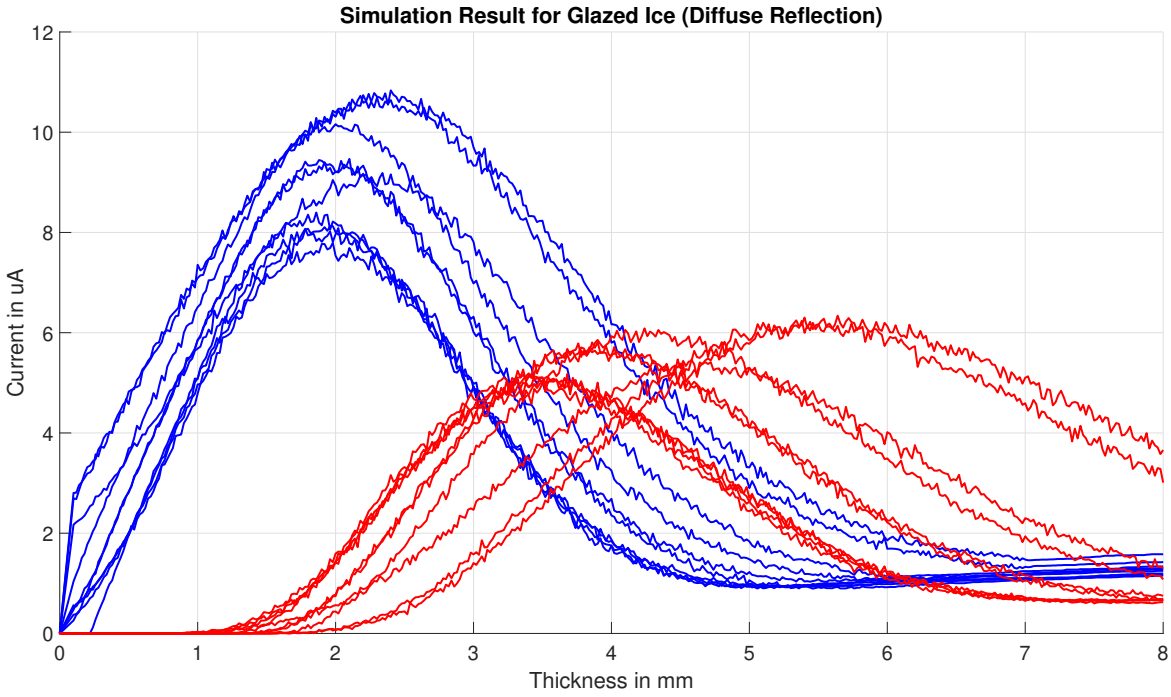

Figure 5.14: Simulation result for glazed ice including additional diffuse reflection at the surface. The diffuse reflection creates a noisy behaviour of the currents I_1 (blue) and I_2 (red) and lowers the overall signal levels.

5.3.4 Rime Ice

In this section the simulation result for rime ice is presented. In order to select according values for the simulation parameters, the results for the measurements, as presented in Section 5.2.2, are again combined in Figure 5.15.

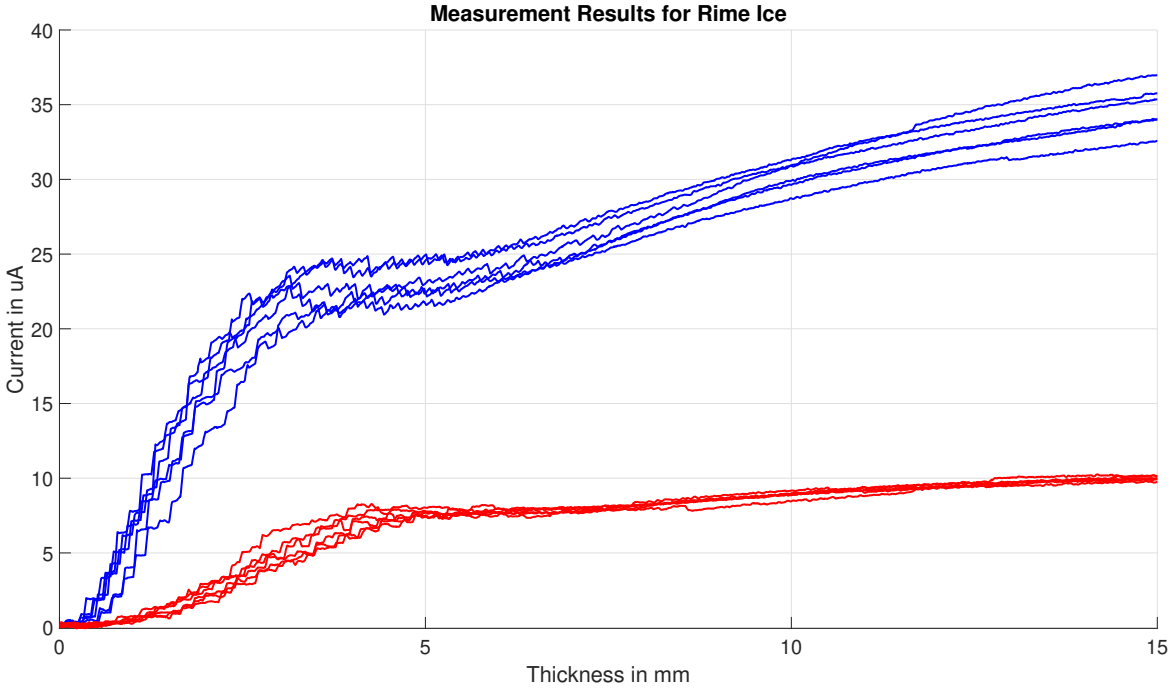

Figure 5.15: Results for measurement experiments for rime ice combined in one plot. The variation between the single currents I_1 (blue) and I_2 (red) for each measurement is illustrated.

It can be seen that the currents for each experiment vary as well. The impact of the surface deviation and the diffuse reflection on the sensor current is seen for thickness smaller than 5 mm. For thickness greater than 5 mm, the diffuse reflection vanishes, as the entire light is scattered and does not reach the ice/air interface.

The simulation result for rime ice is shown in Figure 5.16. Similar to glazed ice, every single simulation results in different realisations of the currents I_1 (blue) and I_2 (red). For current I_1, the highest variation is observed between 18 µA and 25 µA. For small ice thickness, the surface deviation still has an impact on the resulting sensor signal. For ice thickness greater than 5 mm, the impact of the reflection vanishes, as the currents increase steadily. Although a variation is seen, it is rather small compared to the entire signal range, as the current I_1 obtains values greater then 30 µA for an ice thickness of 15 mm.

For the simulation, the parameters are set as follows:

- $\delta_S \sim \mathcal{U}$(-10°,10°)
- $P_B = 0.21$

The diffuse reflection is not considered, as it is assumed that its influence on the ice surface is not significant for rime ice. Hence, $\delta_R = 0$.

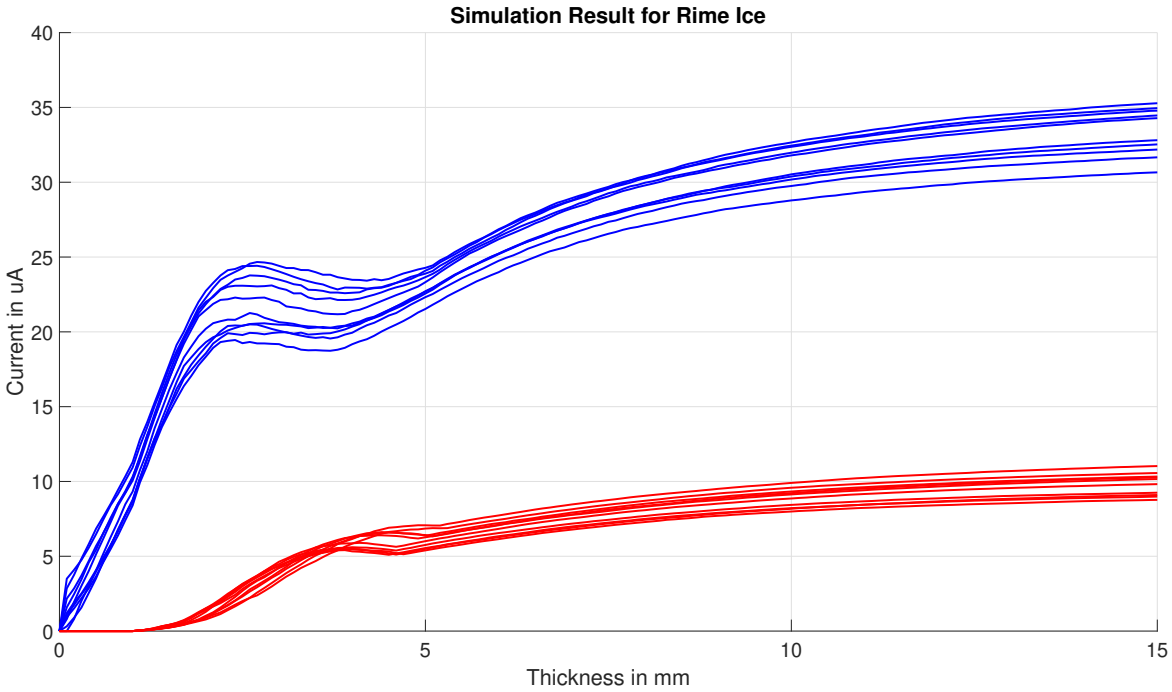

Figure 5.16: Simulation result for rime ice. The variations of the single currents I_1 (blue) and I_2 (red) for each simulation can be seen. The largest variation of current I_1 is observed for an ice thickness between 2.5 mm and 5 mm. In this range, the reflection still has an impact. For a further increase of the thickness, both currents increase steadily.

The result of the simulation and the measurements show good agreement and low variations. For rime ice, an estimation of the ice thickness appears to be possible.

5.4 Uncertainty Evaluation for Thickness Measurement

In this section, an uncertainty evaluation with respect to the thickness measurement is carried out, using the sensor model [5]. In order to obtain a statement about the uncertainty, at first a Monte Carlo (MC) simulation is performed for rime ice.

1000 simulations for rime ice are performed and plotted in a single diagram. The parameters are the same as presented before. For each thickness, the mean and the standard deviation of the currents are computed. The result is depicted in Figure 5.17.

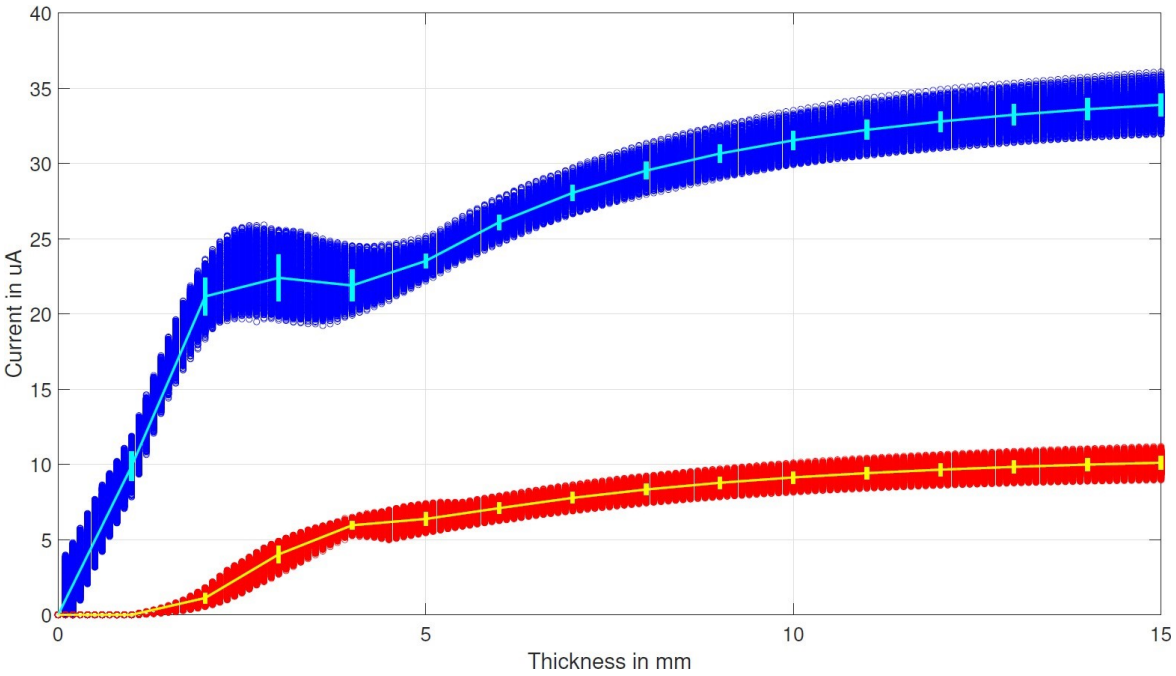

Figure 5.17: Result of the MC simulation for uneven rime ice accretion. The mean and the uncertainty for the currents I_1 (blue) and I_2 (red) can be evaluated, and a statistical model by means of $\boldsymbol{\mu}(d_{\mathrm{Ice}})$ and $\boldsymbol{\Sigma}(d_{\mathrm{Ice}})$ can be derived.

The blue dots represent the samples for each simulation for the current I_1. The cyan curve is the computed mean for each thickness and the cyan vertical bars represent the standard deviation in each millimetre of ice thickness. The red dots are the simulated samples for the current I_2. Their mean and the standard deviation is represented by the yellow curve and its vertical bars.

On the basis of this statistical analysis, the mean $\boldsymbol{\mu}(d_{\mathrm{Ice}})$ and the covariance matrix $\boldsymbol{\Sigma}(d_{\mathrm{Ice}})$ can be constructed.

Once the statistical signal model is given, the uncertainty of the thickness measurement can be represented using the Cramer Rao lower bound (CRLB) [24].

For the computation of the CRLB the mean $\boldsymbol{\mu}(d_{\mathrm{Ice}})$ is approximated by polynomial functions. These functions are used to evaluate the required derivatives. The result of the CRLB is depicted in Figure 5.18.

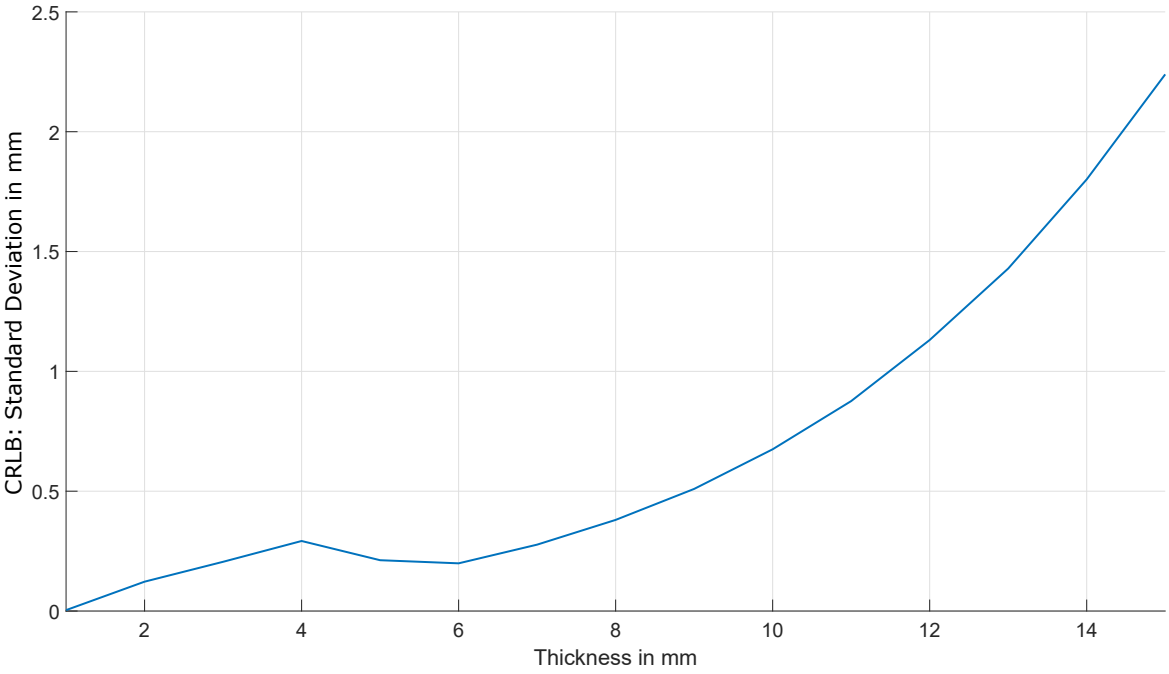

Figure 5.18: CRLB result for ice thickness estimation for rime ice. For increasing ice thickness also the uncertainty regarding the random ice accretion increases.

Measurement noise, the impact of the ambient light or other influences are not considered by the CRLB. It represents the lowest possible uncertainty for the thickness estimation of natural ice accretion.

6 Conclusion and Outlook

The concluding chapter summarizes the results obtained in the course of working on this thesis. Finally, an outlook is given, which provides further aspects in possible future works.

6.1 Conclusion

In this thesis, the sensor effect used for a FOIS is studied. It includes an analysis of how natural ice and its random accretion process affect the sensing principle of the sensor and its capability of

- detecting early ice accretion and
- measuring the ice thickness.

In order to evaluate the sensing tasks as mentioned above, a simulation framework is set up, and one possible sensor structure is studied. The simulation framework uses a Ray-Tracer to describe the propagation of light inside the ice volume. The natural accretion process of ice is represented by a random surface deviation, including diffuse reflection and the different types of ice.

Prototypes of a FOIS are constructed, and a measurement-based characterization of the sensors is performed. Series of experiments are carried out in a climatic chamber in order to ensure the ambient conditions for both glazed ice and rime ice. The documented measurement results are compared with simulation results in order to calibrate the model for future analysis. The results of the measurements and simulations are used for an evaluation of the capabilities to detect ice and measure the ice thickness for glazed ice as well as for rime ice.

Glazed Ice

The capability to detect early ice accretion depends in which way the sensor is constructed. It is shown that a transparent separation of the bundles results in a significant offset of the sensor signal, which makes it difficult to clearly identify a thin ice layer on the sensor. An improvement is provided by using an opaque tape between the bundles. Due to the optical shielding of the bundles, the offset is no longer present and the accretion of ice leads to an initial increase of the sensor signal, making it more efficient for detecting glazed ice accretion at an early stage.

The simulation and also the results of the measurement experiment for glazed ice show that a determination of the thickness is not possible. The sensor signals depend significantly on the surface deviation. As hardly any air is trapped inside the clear ice, the reflection of the ice/air interface is responsible for the amount of detectable light on the signal bundle areas. For each accretion process, the surface of the ice looks different, leading to a high variation of the sensor signal. The diffuse reflection is an additional random factor, which makes the signal appear noisy.

The cross-sensitivity with respect to water for glazed ice is also demonstrated in this work. Since water has similar optical properties to ice, it is not possible to distinguish between water and glazed ice.

Rime Ice

The capability of detecting rime ice on the sensor is similar to glazed ice. Once the bundles are optically separated, an initial increase of the sensor signal can be noticed. Due to the particular composition of the ice volume, the initial increase of the sensor signal is even higher, making it easier to detect ice accretion at an early stage.

With regard to the measurement of the ice thickness, the variation of the sensor signals is again studied. The simulation and also the results of the measurement experiments show that the sensor signal varies as well, but the deviations remain within a tolerant range. Thus it can be concluded that thickness measurement should be possible.

For rime ice, a Monte Carlo simulation and a subsequent evaluation of the CRLB is presented. The uncertainty of the thickness measurement regarding natural ice accretion is shown.

6.2 Outlook

The investigation of the sensor capabilities were carried out in a laboratory environment. The evaluation of the sensor behaviour was a static investigation. In order to gain more information about the ice and its accretion process, an extended study using field experiments can be done in the future.

For the use of this sensor in the field, a sensor fusion with a temperature sensor is required. Sensor fusion is a possible approach to decrease the cross-sensitivity with respect to water in order to make a clear distinction between water and ice.

Another challenge for future research is the impact of ambient light. The sensor is constructed with two signal bundles for a possible further differential evaluation of the sensor signal. An electronic circuit or signal processing can be used to cancel the influence of the ambient light.

A further possible work would be the analysis of the accreted ice. By means of a FOIS it should be feasible to reconstruct the local composition of the ice.

Bibliography

[1] K. Savadjiev and M. Farzaneh. Modeling of icing and ice shedding on overhead power lines based on statistical analysis of meteorological data. *IEEE Transactions on Power Delivery*, 19(2):715–721, April 2004. ISSN 0885-8977. doi: 10.1109/TPWRD.2003.822527.

[2] V. T. Morgan and D. A. Swift. Effect of ice loads on overhead-line conductors. *Electronics and Power*, 11(1):22–23, January 1965. ISSN 0013-5127. doi: 10.1049/ep.1965.0008.

[3] Matthew Homola, Per J. Nicklasson, and Per A. Sundsbø. Ice sensors for wind turbines. *Cold Regions Science and Technology*, 46:125–131, 11 2006. doi: 10.1016/j.coldregions.2006.06.005.

[4] K. Reich, O. Oberzaucher, H. Hopitzan, and G. Brasseur. Ice monitoring at austrian power grid status and outlook, 2019.

[5] Markus Neumayer, Thomas Bretterklieber, and Matthias Flatscher. Signal processing for capacitive ice sensing: Electrode topology and algorithm design. *IEEE Transactions on Instrumentation and Measurement*, 68:1458–1466, 2019. ISSN 0018-9456. doi: 10.1109/tim.2018.2882116.

[6] Umair Mughal, Muhammad Virk, and Mohamad Mustafa. State of the art review of atmospheric icing sensors. *Sensors and Transducers*, 198:14, 03 2016.

[7] A. Troiano, E. Pasero, and L. Mesin. New system for detecting road ice formation. *IEEE Transactions on Instrumentation and Measurement*, 60(3):1091–1101, March 2011. ISSN 0018-9456. doi: 10.1109/TIM.2010.2064910.

[8] L. K. Baxter. *Capacitive Sensor Basics*, chapter DOI: 10.1109/9780470544228.ch3. IEEE, 1997. ISBN 9780470544228. doi: 10.1109/9780470544228.ch3. URL `https://ieeexplore.ieee.orghttps://ieeexplore.ieee.org/document/5312316`.

[9] M. Flatscher, M. Neumayer, T. Bretterklieber, and B. Schweighofer. Measurement of complex dielectric material properties of ice using electrical impedance spectroscopy. In *2016 IEEE SENSORS*, pages 1–3, Oct 2016. doi: 10.1109/ICSENS.2016.7808533.

[10] M. Flatscher, M. Neumayer, and T. Bretterklieber. Field sensor analysis for electrical impedance spectroscopy based ice detection. In *2017 IEEE SENSORS*, pages 1–3, Oct 2017. doi: 10.1109/ICSENS.2017.8234035.

[11] Y. Ma, H. Yu, J. Liu, and Y. Zhai. Measurement of ice thickness based on binocular vision camera. In *2017 IEEE International Conference on Mechatronics and Automation (ICMA)*, pages 162–166, Aug 2017. doi: 10.1109/ICMA.2017.8015806.

[12] Yingtong Liu, Xianggen Yin, Jian Xu, and Zhenxing Li. Mechanical monitoring and risk assessment under ice disaster based on wireless sensor network. In *Proc. IEEE Power Engineering and Automation Conf*, volume 2, pages 229–232, September 2011. doi: 10.1109/PEAM.2011.6134944.

[13] Luming Li, Xin Sun, Xiaobo Meng, Zhiguo Zhang, Xue Chen, and Min Zhang. Real-time ice monitoring on overhead power transmission lines with fbg sensor. In *2010 Second IITA International Conference on Geoscience and Remote Sensing*, volume 2, pages 226–229, Aug 2010. doi: 10.1109/IITA-GRS.2010.5603784.

[14] Aris A. Ikiades, David J. Armstrong, and Glen Howard. Optical diffusion and polarization characteristics of ice accreting in dynamic conditions using a backscattering fibre optic technique. *Sensors and Actuators A: Physical*, 140:43–50, 2007. ISSN 0924-4247. doi: 10.1016/j.sna.2007.06.009.

[15] W. Li, J. Zhang, L. Ye, and C. Li. Modelling and experimental study on the fiber-optic ice sensor. In *Proc. Int. Conf. Information and Automation*, pages 1298–1301, June 2009. doi: 10.1109/ICINFA.2009.5205117.

[16] Junfeng Ge, Lin Ye, and Jianhong Zou. A novel fiber-optic ice sensor capable of identifying ice type accurately. *Sensors and Actuators A: Physical*, 175:35–42, 2012. ISSN 0924-4247. doi: 10.1016/j.sna.2011.12.016.

[17] Jianhong Zou, Lin Ye, and Junfeng Ge. Ice type detection using an oblique end-face fibre-optic technique. *Measurement Science and Technology*, 24:035201, 2013. ISSN 0957-0233. doi: 10.1088/0957-0233/24/3/035201.

[18] Jianhong Zou, Lin Ye, Junfeng Ge, and Chengrui Zhao. Novel fiber optic sensor for ice type detection. *Measurement*, 46:881–886, 2013. ISSN 0263-2241. doi: 10.1016/j.measurement.2012.09.020.

[19] W. Li, J. Zhang, L. Ye, and H. Zhang. A fiber-optic solution to aircraft icing detection and measurement problem. In *Proc. Int. Conf. Information Technology and Computer Science*, volume 1, pages 357–360, July 2009. doi: 10.1109/ITCS.2009.77.

[20] Eugene Hecht. *Optics*. Pearson global edition. Pearson, Boston, 5 ed/fifth edition, global edition edition, 2017. ISBN 9781292096933. Authorized adaptation from the United States edition.

[21] Stephen G. Warren, Richard E. Brandt, and Thomas C. Grenfell. Visible and near-ultraviolet absorption spectrum of ice from transmission of solar radiation into snow. *APPLIED OPTICS*, 45:5320, 2006. ISSN 0003-6935. doi: 10.1364/ao.45.005320.

[22] Honeywell International Inc. Sd3443/5443; silicon phototransistor.

[23] LITE-ON Technology Corp. / Optoelectronics. Ir emitter and detector; product data sheet; lte-3271b, 2013.

[24] S. M. Kay. *Fundamentals of Statistical Signal Processing: Estimation Theory*. Upper Saddle River, NJ, USA: Prentice-Hall, Inc., 1993.